Aerospace Science and Technology 177 (2026) 112717

Contents lists available at ScienceDirect

Aerospace Science and Technology

journal homepage: www.elsevier.com/locate/aescte

Feasibility and trade-offs in the design of an airship for Martian exploration

Carlo E.D. Riboldi [1,*], Daniele Marcora

Department of Aerospace Science and Technology, Politecnico di Milano, via La Masa, 34, Milano, 20156, Italy

ARTICLE INFO

Communicated by Dr Mehdi Ghoreyshi

Keywords:
Airship design
Mars atmospheric flight
Mission analysis
Trade-off analysis
Design point
Thermal model
Solar cells
Propeller design
Sensitivity analysis
LTA

ABSTRACT

The rapid growth of the field of airship technology over the last few years for Earth missions, in turns enabled by the development of electric motors employed in a distributed fashion as a means for both propulsion and control, is fueling the investigation of the adaptability of this type of flying platform for several tasks. Through the energy harvesting capability achieved with solar cells, the already inherently superior endurance of airships could be extended in principle to the order of months, thus producing a highly-effective platform especially for high-altitude, low-payload monitoring tasks. The spill-over of these analyses to other planetary scenarios featuring a significant atmospheric layer is straightforward - in principle. Several shortcomings affecting the design of airships on Earth have to be analyzed as well in the generally more requiring non-terrestrial environments, coping with additional specific scenario constraints. This research, grounded on a consolidated methodology previously introduced and employed for the sizing of diverse airships for Earth missions, discusses such additional constraints and the features of an airship design procedure needed to cope with them. Furthermore, a specifically emended design methodology is employed to analyze in a parameterized fashion the effect on the airship sizing of some key technology and mission design assumptions, yielding an assessment of the feasibility and critical points. This research is aimed to answering three pivotal questions about the operational feasibility of an airship for Martian exploration. Firstly, to what extent can established sizing frameworks for terrestrial high altitude airships be adapted to the Martian environment. Secondly, what are the primary technological constraints that dictate the overall feasibility of the concept. Finally, whether a solar-powered design optimized for a specific mission, in favorable yet realistic conditions, be achievable. When placed in the context of the available literature concerning Martian airships, this work provides a clear insight on the global feasibility of such a mission, highlighting the technological bottlenecks possibly preventing the practical realization of an LTA concept for Martian exploration.

1. Introduction

Far from being a surpassed platform for atmospheric flight, airships are currently gaining once again the interest of industry and scientists. Their inherent longer flight endurance compared to other atmospheric flying machines, resulting from the employment of buoyancy in lieu of dynamic lift as a major element for supporting weight, can be effectively coupled with a fully-electric propulsion and attitude control system, based on electro-mechanic actuators (i.e., servo-motor and propellers), suitably positioned on-board in a distributed fashion. This feature, together with consolidated on-board computers, now cheaply available in many options, produces a favorable framework for improving disturbance rejection (in particular, from wind oscillations) and in general controllability [1–3], which used to constitute a major shortcoming specifically to airships.

As witnessed by the current most developed endeavors for terrestrial application, airships can be employed competitively with respect to other atmospheric flight machines especially on two missions. Firstly, at very low altitude, and with a limited (non human) payload, for monitoring and surveillance missions [4–9]. In this form, airships are relatively simple to design and manufacture, hence they are becoming increasingly consolidated as credible competitors to multi-copter UAVs, which are enormously weaker in terms of endurance [10]. Secondly, airships are being studied very actively for high-altitude missions, typically in the terrestrial stratosphere (i.e., 18–20 km above ground) [11–15]. The ability to accurately position, orient and potentially recover the payload are valuable advantages offered by airships more than potential competitors, in particular low-orbit space satellites. Furthermore, the adoption of high-performing solar cells, coupled with the intense Sun radiation levels in the stratosphere, allows to harvest an amount of

* Corresponding author.
E-mail address: carlo.riboldi@polimi.it (C.E.D. Riboldi).
[1] www.riboldiresearch.net.

https://doi.org/10.1016/j.ast.2026.112717
Received 4 February 2026; Received in revised form 27 May 2026; Accepted 27 May 2026
Available online 30 May 2026

Table 1
Average nominal atmospheric and environmental features of Venus and Mars (on the surface). [18].

Planet	Gravity [m/s^2]	Temperature [K]	Pressure [bar]	Density [kg/m^3]	Composition
Venus	8.93	735	9.21	65	CO_2 97%, N_2 3%
Mars	3.73	220	6.36	0.02	CO_2 95%, N_2 3%, Argon 2%

energy sufficient for supplying the power systems and the payload of a high-altitude airship (HAA) during the day, while also reloading accumulation systems for the night. This would extend the mission time to the level of months or even years. In this second scenario, airship technology is not yet mature, in particular due to the challenging requirements of the climb phase, which requires enhanced buoyancy control and structural resistance, which in turn produce rather large and expensive sizing solutions.

The attitude of the industry in the field of airships currently mostly reflects the good practice of finding niches where the weaknesses of existing solutions are compensated by the strengths of these alternative platforms. This standpoint can be adopted to evaluate other potential scenarios of employment, in particular in extra-terrestrial environment.

The use of lighter-than-air technology for missions on foreign bodies in the solar system is not new. When considering in particular the collection of data from the surface, in those cases where atmospheric flight is at all possible, airships offer a platform ideally bridging between the low-resolution data provided by high-altitude orbiters on very large sectors, and the high-resolution and direct sampling obtained on a very limited area from rovers [16]. Considering gaseous planets are mostly composed of Hydrogen, and most moons have very tenuous atmospheric layers, which offer only a residual buoyant capacity and dynamic pressure (except for very high airspeed values), atmospheric flight in the solar system is mostly of interest only on Venus and Mars [17]. The features of these two potential scenarios for atmospheric flight will be synthetically reported now, including previous studies and flight attempts.

1.1. Atmospheric flight on Venus

The thick atmosphere of Venus (Table 1) in principle favors atmospheric flight, and in particular lighter-than-air technology.

The predictability and limited oscillation of the wind and the high radiation intensity due to the increased proximity with the Sun compared to the Earth, are favorable factors for airship flight [18]. In particular, the thick layer of sulfuric acid clouds which partially reduces solar radiation for reduced altitudes, allows for a sweet spot at 45–64 km, where some atmospheric conditions similar to those found in Earth's troposphere are encountered (i.e., pressure ∼1 bar, temperature ∼300 K) [17]. In that condition, recharging the energy storage systems is possible thanks to solar energy harvesting, thus allowing for a prolonged mission time. However, the intensity of wind, ranging between the tens and hundreds meters per seconds, depending on altitude, is generally too high for station-keeping, i.e. for constantly overflying a specified position on the surface. Additionally, the aggressive atmospheric chemical and thermal conditions in the lower layers of the atmosphere are a well-known issue, imposing significant degradation rates on components, and calling for a reduction of the time spent in that environment to increase the survivability of the flying platform.

For these reasons, up to our days, atmospheric flight on Venus has been carried out or planned employing LTA technology, but with non-controlled balloons instead of airships, to the aim of overflying large portions of the surface, renouncing to station-keeping, and exploiting the winds to carry out a passive sampling mission. The first such attempt is constituted by the Vega balloons in 1985, which carried a payload under 25 kg each for atmospheric sampling [19]. Incapable of energy harvesting, these battery-fed payloads operated for up to 47 h, while flying an over-ground trajectory of up to 11,000 km, by exploiting the intense winds. They were released from the descent module at 65 km, inflated with Helium and descended to a target floating (i.e., buoyancy-weight equilibrium) level at 54 km. More recently, project VALENTInE was developed as a long-endurance, variable altitude mission, to sample the lower layers of the atmosphere [20]. In this case, a Helium-inflated balloon stationing at 55 km has been designed to be able to carry out five dip maneuvers down to 45 km, each lasting 3 h, and coping with high temperature constraints. Notably, the payload of the balloon, highly detailed in the mission planning in view of the sampling to carry out, weighs close to 20 kg.

1.2. Atmospheric flight on Mars

The ground density of the atmosphere on Mars is roughly two orders of magnitude below Earth's value (i.e., comparable to the Earth's value between 30-40 km) which makes atmospheric flight, either lighter or heavier than air, generally more requiring either in terms of power or buoyant volume, for the same payload, with respect to Earth's troposphere (Table 1). Winds are generally predictable, and range between less than 10 m/s, measured at the Viking landing site, to the 50 m/s estimated on top of the surface boundary layer, a value comparable to those encountered in the stratospheric layers of Earth's atmosphere. Notably, these features constitute a loosely comparable, yet less requiring scenario with respect to the terrestrial stratospheric conditions. The orbital mechanics of the planet, featuring a spinning axis not normal to the ecliptic plane, similar to the Earth produce seasonal changes in the solar radiation angle and the daylight time, for a given position on the surface. Considering a self-sustaining airship application for station-keeping, forcibly based on solar energy harvesting, and required to counter the wind intensity corresponding to a given position and altitude, the selection of a specific position over the surface is relevant to guarantee the feasibility of the mission profile (i.e., primarily energy balance), similar to the stratospheric applications on Earth. Actually, largely predictable atmospheric phenomena, where intense dust storms obfuscate sunlight for half of the year (autumn and winter), constitute a further constraint in the choice of the positions over the surface where a station-keeping mission can be carried out [21,22].

The existing similarities between Mars and Earth, and the ensuing scientific interests and prospective colonization opportunities condensed in the MEPAG milestones [23], have driven an increased attention to the exploitation of existing technologies for the Martian scenario. In facts, atmospheric flight has been already attempted, notably with the heavier-than-air Ingenuity helicopter [24]. Weighing 1.8 kg and featuring a rotor diameter of 1.21 m, and embodying solar cells for battery recharging, this platform could achieve a flight time of 90 s. It carried out 72 flights between 2021 and 2024, and despite largely surpassing its goal as a conceptual demonstrator for VTOL operations on a foreign planet, it only flew for a total of 128 min and 17 km range. Next generation Mars Science Helicopters (MSH), also employing a multi-rotor design, are planned to increase payload (5 kg), range (5 km) and endurance (10 min in hovering), without raising the diameter of the rotors beyond 2.5 m [25]. Concerning lighter-than-air flight, preliminary investigations have been carried out by Girerd for a non-rigid airship [26], carrying a payload of 10 kg on a range in excess of 1,400 km at 10 m/s. The sizing procedure forecast a length of about 50 m, and an overall weight of 199 kg. Similar to the later project MARVIN, developed for high-resolution mapping in search for methane [27], propulsion was non-electric, as mostly typical in atmospheric flight before the last 15 years as already pointed out. Further studies include the evacuated concept within the NIAC program [28], which brings in the shortcoming of the unassisted rigid balloon assembly and sealing, as well as the transportation of its components, and the work by Colozza [18], who investigated the feasibility of a solar-powered balloon with solar energy harvesting capability, employed to feed a regenerative fuel-cell system, and concluding that a mission requiring station-keeping would produce a machine with a hardly acceptable sizing, with the technology of the time for solar energy harvesting, energy storage and airship envelope making. The recent research of Pozhanka and Hassanalian [29] revamps the concept of an airship application to exploration mission. Operating at an altitude of 2,000 m, 10 m/s and a payload of 25 kg, the sizing calls for a nearly 100 m machine. The work does not pose constraints on the energy efficiency of motors and propellers, and assumes highly-efficient solar cells/regenerative fuel cells.

1.3. Research outline

The present research aims at investigating further the feasibility of an airship for a monitoring mission on a foreign planetary body. The preliminary analysis of the environmental conditions just recapped for Venus and Mars suggests that the Martian scenario offers a better chance to exploit the abilities of an airship compared to other LTA platforms, in particular due to the lower intensity of the wind on Mars. In the latter case, the ability of the airship to position autonomously and keep over an assigned point could be exploited, and the presence of a ground base would allow mounting and resupply, even in an automated fashion, i.e. without human intervention. The availability of such a base, albeit unmanned, appears significantly closer in time on Mars than on Venus. As a matter of fact, Mars is in the focus of a more direct interest from the community, as stated in the MEPAG road map, and as witnessed by the multiple studies and application of atmospheric flight cited above.

The analysis presented herein is based on a purpose-developed version of a preliminary design methodology for airships, implemented in the proprietary code `Morning Star`. Originally developed and extensively employed for the sizing of airships on Earth, this methodology is here emended to bear results in the Martian environment. The workflow of the code, described in detail elsewhere [13], will be summarized in a dedicated section. Notably, the baseline procedure required for the sizing of a stratospheric airship on Earth is very similar to that needed for designing a low-altitude airship on Mars. The low density of the atmospheric air, the predictability of the wind and the significant exposure to solar radiation are typical to both scenarios, when considering the airship in a long-lasting cruising phase. The methodology previously available in `Morning Star` was however amended substantially in this work, in order to more accurately model some aspects of the airship. In particular, these modifications include the topological and thermal modeling of solar cells, the design of a propeller, besides environmental changes, like the detailed definition of the Martian atmospheric conditions, including wind and solar irradiance. Furthermore, the effect in terms of weight of a buoyancy management system, interesting for a realistic management of the altitude over a mission, is considered explicitly, even though only through a very simple model.

After defining a detailed candidate mission profile, a parameterized analysis has been carried out, running the sizing method systematically while concurrently changing significant settings, representing technological choices. The corresponding sizing results will not only show the generalities of a sizing solution for Mars, accounting for realistic technologies, but also the effect of some technological choices on the sizing, thus evidencing bottlenecks in the potential practical making of an airship platform for atmospheric flight on Mars.

2. Baseline sizing methodology

The adopted airship sizing methodology, firstly introduced to size up a high-altitude airship (HAA) for Earth observation deployed with a missile (the *satelloon* concept) [13] and subsequently amended for diverse applications (i.e., low altitude [7], different types of propulsion [14,15], with or without solar cells [10]), is based on two logical components, namely a *sizing loop* and an *optimum-seeking layer*. The sizing loop allows to start from a set of specifications (e.g. the length of the airship, or the geometric features of the solar cells), and through the inherent features of the technologies selected for the design (e.g., the material of the envelope, or the quality of the lifting gas), it allows to obtain a corresponding candidate sizing via explicit, closed form expressions. The resulting candidate sizing however is not necessarily compliant with respect to three requirements, namely dynamic lift and buoyancy vs. weight of the machine, balance of power in each and every phase of the mission, and structural integrity. The optimum-seeking layer, on the other hand, automatically steers the set of specifications of the sizing loop towards minimum weight, while simultaneously putting the three requirements just mentioned as numerical constraints on the solution. A visualization of the complete algorithm is presented in Fig. 1.

In order to better appreciate the changes to the baseline algorithm included in this research, the sizing procedure just outlined, implemented in a suite called `Morning Star` and already discussed elsewhere (see in particular [13,15]), will be recapped synthetically here.

2.1. Outline of the sizing procedure

Referring to Fig. 1, the sizing loop allows for the computation of a candidate sizing solution, starting from a set of variables wrapped in array $\boldsymbol{p}$, which will be iteratively changed by the optimum-seeking loop, and accounting for several specifications which will be held constant in the process.

The set of variables in $\boldsymbol{p}$ is kept to a minimum, to reduce the order of the optimization process. A shape function is employed for assigning the geometry of the envelope. The choice of the shape function defines the number of parameters required for assigning a corresponding sizing. In this work, a simple bi-ellipsoidal shape has been considered, which can be translated into a geometrical sizing by assigning the length of the envelope L and the fineness ratio f, where the latter is $f = \frac{L}{D_{\max}}$, and $D_{\max}$ is the top diameter of the envelope. Additionally, four sizing parameters are defined, related to the solar cells. These are assumed to be placed on board in two symmetric arrays, one on either side of the envelope, adapting to the envelope surface and following its three-dimensional geometrical curvature, with a longitudinal extension between stations x_{le} (leading-edge) and x_{te} (trailing edge), and an angular extension (one side) between θ_{in} and θ_{out}. The meaning of these parameters is graphically explained in Fig. 2. Altogether, the array of parameters is defined as $\boldsymbol{p} = \{L, f, x_{le}, x_{te}, \theta_{in}, \theta_{out}\}$.

The parameters to be assigned for running the sizing loop can be split into four categories:

1. *Mission parameters*. Similar to aircraft, these include the ground speed and altitude change for climb and descent, as well as the ground speed, altitude and duration of the cruise phase. For a station-keeping mission, which will be in the focus of the applicative Section 4 in this work, the airspeed is non-zero, even though the ground speed is null, on account of a non-negligible wind. In addition, the geographical position of the mission starting point and of the station to be kept (i.e., for station-keeping) need to be specified. These parameters are pivotal in assigning the thermodynamic condition of the atmospheric gas mixture, as well as the solar irradiance. It should be noted that the airship is assumed to keep horizontal and in an attitude where the plane of symmetry is aligned with the direction of the wind, in order to minimize drag with respect to a side-slipped condition. This assumptions define the mutual direction of the solar rays with respect to the solar panels. Changes to these settings in the newly adapted version of the code to cope with the Martian environment will be treated in Sections 3.1, 3.2.
2. *Payload parameters*. The payload is characterized by its own mass and power required. For the case at hand, some details will be added for a specific mission in Section 4.4.1.
3. *Technological parameters*. Envelope and systems parameters relate sizing parameters to mass, through statistics-based regressions or first-principle models. Quantities to be assigned include the top acceptable wind speed for envelope sizing, the

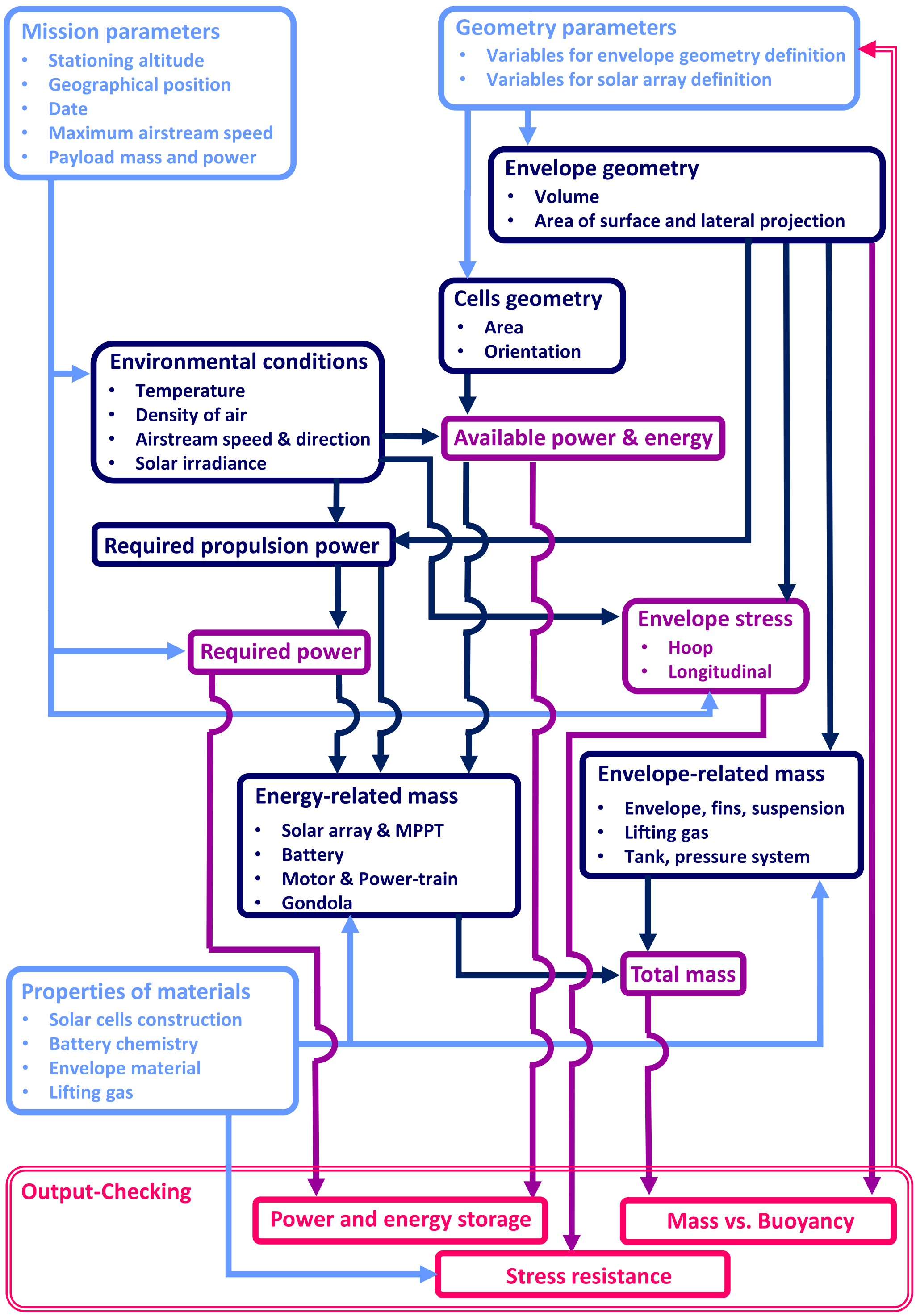

Fig. 1. Chart of the baseline `Morning Star` conceptual workflow.

identity of the envelope material, specified through its areal density and top-stress characteristics (which are typically related via a technological regression), and the thermodynamic properties of the lifting gas including purity level. Similarly, characteristics of the fins, septa, and stringers are specified, in terms of relations linking their geometrical sizing to their mass. Ballonets, buoyancy control devices required to cope with changing atmospheric conditions (typically, but not only, observed in a climb, as will be exhaustively shown in this research), are not included in the original implementation, and will be discussed in Section 4.4.3.

4. *Power and propulsion systems*. Assigning the chemistry of the battery yields specific energy and specific power characteristics. Solar array technology implies values of mass density and energy conversion efficiency of its layers. This part, treated in a simplistic way in the original implementation, will be addressed thoroughly in this research, due to its relevance for a Martian application (see Section 3.4). Mo-

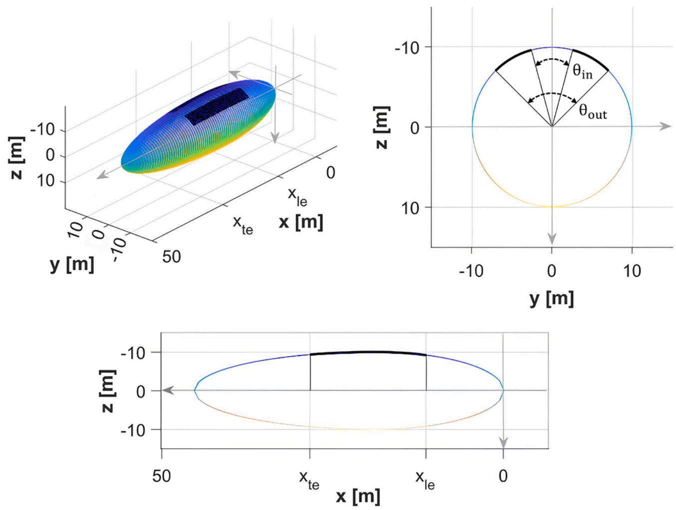

Fig. 2. Example schematic representation of the geometry of the envelope and of the solar array layout from `Morning Star`.

tor characteristics include the conversion efficiency of the electric motor and the propulsive efficiency of the propeller. A potentially critical parameter for the Martian environment, the analysis of a propeller dedicated to the application at hand will be presented in Section 4.4.4.

2.1.1. Sizing loop

Referring again to Fig. 1, the passages implemented to complete the sizing loop are concisely mentioned here.

1. *Geometrical sizing of envelope*. The knowledge of L and f allows to define the sizing of the envelope, based on the shape function describing its geometry. Correspondingly, the other parameters in $\boldsymbol{p}$ allow to define the sizing and local orientation of the solar arrays. The sizing of the envelope enables the estimation of the drag and lift characteristics, and by triggering the sizing of the tails, it also enables the computation of major static stability derivatives.
2. *Computation of environmental conditions*. Based on the settings of the mission profile, including in particular the geographical location and start time of the mission, the atmospheric (including wind) and irradiance conditions are defined. Their evolution along a mission of a certain duration, due to day and seasonal effects e.g. for a station keeping mission lasting several days or even months, is accounted for as well.
3. *Computation of required power and energy*. From the user's defined parameters assigning the mission profile and the aerodynamic characteristics of the environment, the drag required along the mission is obtained, as a discrete function of time. Power needed for propulsion is correspondingly computed, and added to the power needed for the payload.
4. *Computation of power available, power balance and sizing of energy storage*. The power available is computed as a function of time from the knowledge of the position and orientation of the airship solar arrays over time, and the orientation of the incoming radiation on the other. The knowledge of the power required vs. power available at any time enables the computation of a power flow from/to the energy storage system, i.e. the batteries in this implementation. Both energy and power limits associated with the assigned technology and current sizing of the battery within the loop are considered for the sizing. From a knowledge of the power balance all along the mission, and assuming an initial state of charge of the batteries, the energy to be stored in the batteries at any time such to satisfy the power balance can be computed, and from it the top value of the energy in the batteries. Similarly, the top value (either charging or discharging) of power that the batteries should manage can be computed. These data enable the computation of the battery mass m_{bat}, according to the most stringent requirement among maximum energy and maximum power that the battery should manage.
5. *Computation of mass of the power system*. The power required for flight allows the assignment of the power of the motors and propellers. These are turned into corresponding masses m_m, which are complemented by those of the power-trains and sub-plants (cables, power electronics, etc.), wrapped in m_{el}. Finally, the mass of the power system includes that of the batteries m_{bat} and solar cells m_{sc}, obtained starting from their respective sizing (see previous points).
6. *Structural stress computation*. The knowledge of the outside total load (i.e., static and dynamic) and of the thermodynamic state of the lifting gas allows to compute the top pressure differential over the envelope, and from simple models the hoop stress and longitudinal stress to be achieved, to avoid structural failure within the envelope.
7. *Mass of envelope and structural components*. The sizing of the envelope including its thickness allows to define its overall mass m_{env}. The volume of the envelope and the pressure in it allow to define the mass of the lifting gas m_{lg}. Finally, the masses of structural parts like the fins (m_t) and inner septa (m_{str}) are computed as functions of the size of the envelope.

At the end of the sizing loop, the overall mass of the airship can be computed by summing mass components as

$$m = m_{env} + m_{lg} + m_{bal} + m_{sc} + m_{bat} + m_m + m_{el} + m_{str} + m_t + m_{pl}, \quad (1)$$

where m_{pl} is the assigned mass of the payload and m_{bal} the mass of the ballonet system (where present).

2.1.2. Optimum-seeking loop

The optimum-seeking loop automatically changes the set of parameters $\boldsymbol{p}$, looking for the sizing solution with minimum mass m, such to satisfy the following constraints.

1. *Weight balance*. The actual buoyancy ratio of the airship can be computed all along the mission profile, and constrained to be above a prescribed minimum value, thus ensuring the sustainment of the airship.
2. *Integrity*. The maximum stress recorded along the mission profile (see the sizing loop) should never exceed a prescribed technological maximum, obtained from the characteristics of the selected envelope material.
3. *Battery energy and power balance*. For the current sizing, as set by the sizing loop, the power and energy stored in the battery are checked along a simulated mission profile on a discrete time grid, to verify the ability of the batteries to supply sufficient power to the motors and payload at any time, without reaching a complete discharge condition on one end, and such to avoid exceeding a fully-charged state of charge on the other.

The so-configured optimum-seeking problem features a good regularity both in terms of cost function and constraints, and it can be managed successfully with a standard gradient-based algorithm.

3. Modifications to the baseline airship sizing methodology for a Martian mission

Some modifications to the procedure originally prepared for the terrestrial case and recalled in Section 2 are needed to cope with the different environment found on Mars, in terms of atmospheric conditions and solar irradiance. An accurate modeling of both these conditions is crucial, since the sensitivity of the sizing solution to the environmental setting is often critical [7]. Furthermore, on account of the more extreme variations of the atmospheric conditions over time found on Mars compared to planet Earth and on the major role of hi-technology solar cells in the application at hand, a thermal modeling of the solar arrays and of the envelope material has been carried out, so as to enable a sufficiently accurate computation of their respective properties over the mission time frame. The models and procedures envisaged for these tasks will be reported in the next paragraphs.

3.1. Atmospheric environment on Mars

As a primary source of atmospheric data for Mars, the Mars Climate Database (MCD) [30] has been employed. This is a semi-empirical, statistics-based model developed for Mars. It takes into account the most impacting known phenomena, namely atmospheric circulation in three-dimensions, radiative transfer through gases and aerosols of dust and ice, Carbon-dioxide and water cycles, dust convection and photochemistry of the atmospheric mixture. The model spans between the surface and an altitude of 300 km, and it has been validated using available observation data [31].

For the design task at hand, the model can be queried, setting as input the surface coordinates and altitude of the airship, and the time coordinates, namely the solar longitude of the planet L_s along its orbit and the Martian hour of the day. The model then returns the values of the thermodynamic state variables, density ρ_{atm}, temperature T_{atm} and pressure P_{atm}, as well as the local wind components in a northern and eastern direction, $V_{w,N-S}$ and $V_{w,E-W}$ respectively. As stated above (Section 2.1.1), by hypothesis the airship is kept aligned with the wind, which is reasonable so as to minimize drag. Therefore, the knowledge of the wind vector also defines the orientation of the airship, hence the mutual attitude with respect to the solar radiation.

Notably, for a station keeping mission, the position of interest can be assigned as a single point on the surface, and a time profile for each of the output variables just mentioned can be obtained for a discrete set of altitudes, relevant for the mission profile of the airship.

In addition to the quantities directly retrieved from MCD, dynamic and kinematic viscosity, as well as the speed of sound, which are needed for aerodynamic (i.e., at the level of accuracy of preliminary sizing, for determining aerodynamic coefficients from regressions) and thermal computations (see Section 3.4), can be obtained from the application of Sutherland's law [32], and from the ideal gas hypothesis, employing the available values of the adiabatic index and gas constants for Mars [33].

A relevant practical outcome of a preliminary analysis carried out on the behavior of thermodynamic quantities on Mars is related to the density ρ_{atm}, which is a pivotal quantity for atmospheric flight and especially for buoyancy. For a sample position on the northern polar cap of Mars, which will be treated later for practical computations (see Section 4.4.3), a relevant excursion of ρ_{atm} equal to 40% of its nominal value is observed, between a solar longitude of $L_s = 45°$ and $L_s = 135°$. Conversely, the change in density over a day cycle is negligible. The intense low-frequency (i.e., seasonal) change of the density suggests that for a mission extending over time on a comparable time frame, a buoyancy management system would be strictly needed for an airship to be able to cope with the changing environmental conditions, thus in particular keeping at a constant altitude over time.

3.2. Solar radiation on Mars

As the only source of power enabling the extension of an airship mission over a time frame sufficient for making it a realistic monitoring or prolonged sounding platform, solar power harvesting needs an accurate modeling, accounting for the dependence of captured solar irradiance from the solar longitude of Mars, the time of the Martian day, and from the position of the airship on the planet. Later, the geometrical and technological features of the solar cells and their effect in the harvesting process will be considered (Section 3.4).

A baseline methodology for the task is documented in [34]. However, for increased accuracy, the procedure has been extended so as to accurately account for the optical depth and albedo parameters on Mars, as described in the following.

In a North-East-Down (NED) local frame centered in the airship on Mars, the direction of the Sun beams at any time (in particular, pointing from the origin of the frame to the Sun) can be assigned with the unit vector in Eq. (2),

$$\boldsymbol{s}_{sun}^{NED} = \left\{ \cos\psi \sin\vartheta_z, \sin\psi \sin\vartheta_z, -\cos\vartheta_z \right\}, \tag{2}$$

where angles ϑ_z and ψ represent the zenith and azimuth angles of the Sun with respect to the NED reference. These angles can be determined starting from the solar longitude L_s, the Martian hour of the day h, the latitude of the airship ϕ, and the inclination angle e. The latter corresponds to the angle between a direction normal to the ecliptic plane and that of the rotation axis of the planet, and is assumed constant at $e = 24.94°$ [34]. From this data, the declination and hour angles, δ and ω respectively, are computed as in Eq. (3) [35],

$$\begin{aligned} \delta &= \arcsin(\sin e \sin L_s), \\ \omega &= \frac{360}{24}(h-12)\frac{\pi}{180}. \end{aligned} \tag{3}$$

The solar zenith angle ϑ_z can be computed from the latitude ϕ of the point of interest, and from Eq. (3) as

$$\vartheta_z = \arccos(\sin\phi \sin\delta + \cos\phi \cos\delta \cos\omega). \tag{4}$$

The solar azimuth can be computed employing the complementary of ϑ_z, defined as the elevation angle $\vartheta_e = \frac{\pi}{2} - \vartheta_z$, as

$$\psi = \begin{cases} \arccos\left(\dfrac{\sin\delta\cos\phi - \cos\delta\sin\phi\cos\omega}{\cos\vartheta_e}\right), & \omega < 0 \\ 2\pi - \arccos\left(\dfrac{\sin\delta\cos\phi - \cos\delta\sin\phi\cos\omega}{\cos\vartheta_e}\right), & \omega \geq 0 \end{cases} \tag{5}$$

The solar irradiance vector is obtained by multiplication of the direction of the Sun beams, represented by $\boldsymbol{s}_{sun}^{NED}$, by the irradiance intensity. To obtain the latter, first the beam irradiance is evaluated on top of the Martian atmosphere [34], based on the solar longitude (i.e., the position of the planet along its solar orbit), as

$$G_{ob} = \bar{G}\frac{\left(1 + e_c\cos(L_s - \bar{\omega})\right)^2}{(1-e_c^2)^2}, \tag{6}$$

where in Eq. (6) $e_c = 0.09338$ is the eccentricity of Mars orbit, $\bar{G} = 590$ W/m^2 is the average beam irradiance from the Sun on Mars, and $\bar{\omega} = 248°$ is the solar longitude of the perihelion of Mars orbit.

Now, the global solar irradiance reaching a point at a generic altitude within the Martian atmosphere is composed of a direct and a diffuse component.

The direct component of the irradiance G_b at altitude within the atmospheric layer on Mars can be obtained from the Beer-Lambert law, yielding

$$G_b = G_{ob}\mathrm{e}^{-\tau\cdot m(\vartheta_z)}, \tag{7}$$

where in Eq. (7) τ is the optical depth, and the air mass parameter $m(\vartheta_z) \simeq \frac{1}{\cos\vartheta_z}$ represents the mass of air crossed by the beam. The value of the optical depth is not readily available for Mars, except at spot locations. Here the values obtained from measurements on ground by the Viking lander [36] as a function of L_s over an entire Martian year are employed, and interpreted as zero-altitude values of τ_0, irrespective of the position on the surface (the latter is an approximation, since the datum from the Viking lander is only available for its position). Furthermore, the corresponding value τ at a generic altitude z has been computed based on an exponential law [37], yielding

$$\tau(z) = \tau_0 \cdot e^{-\frac{z}{H}}, \tag{8}$$

where, in Eq. (8), $H = 1.11{\cdot}10^4$ m is the scale height within the Martian atmosphere, and represents the altitude change corresponding to a decrease of the pressure by a factor e.

The diffused irradiance component has been estimated as follows. A prediction of the total irradiance on the Martian surface G_h (note, this is computed on the surface, i.e., with an assigned orientation of the receiving surface), based on a mapping by Pollack [38], has been employed for computing the net solar irradiance on ground. This datum is available as a tabulated normalized function $f_i = f_i(\vartheta_z, \tau)$ of the solar zenith ϑ_z, corresponding to the position and time on ground, and of the optical depth on ground τ_0. This normalized function is such that the total irradiance G_h on the Martian surface could be computed as $G_h = G_{obh} f_i$. However, notably the f_i function has been obtained for a specific value of the surface albedo of $a = 0.1$. An approximated estimation of G_h can be obtained for different values of the albedo, yielding a correction of the model just introduced, as

$$G_h = G_{obh} \frac{f_i(\vartheta_z, \tau)}{1 - a}. \tag{9}$$

In Eq. (10), the value of the direct irradiance impacting a horizontal plane on top of the Martian atmosphere is obtained, for a given location, through the corresponding zenith angle of the Sun, as

$$G_{obh} = G_{ob} \cos \vartheta_z. \tag{10}$$

The value of the albedo a in Eq. (9) in the atmosphere is not trivial to estimate, and it is in general a function of the composition of the terrain, being typically higher for the polar ice caps, and lower for dusty terrain. Furthermore, moving to a higher altitude, the value of the albedo is reduced. To account for this, the law proposed by Silk [39] has been employed, yielding

$$a = 0.1 \left(\frac{R_p}{R_p + z} \right)^2, \tag{11}$$

where in Eq. (11) $R_p = 3{,}376.2 \cdot 10^3$ m is the Martian polar radius.

With a knowledge of G_{obh} from Eqs. (6) and (10), the total irradiance on the plane of the horizon G_h at altitude can be estimated making use of Pollack's model via Eq. (9), accounting for the albedo at altitude from Eq. (11) and the optical depth at altitude from Eq. (8). Correspondingly, the direct beam irradiance on the same horizontal plane can be computed, similar to Eq. (10), as

$$G_{bh} = G_b \cos \vartheta_z. \tag{12}$$

Finally, this allows to obtain the diffused irradiance on the horizontal plane at altitude G_{dh}, by subtracting the direct irradiance on a horizontal plane at altitude G_{bh} from G_h, or analytically

$$G_{dh} = G_h - G_{bh}. \tag{13}$$

In order to compute the intensity of the radiation entering the solar array, the geometrical modeling of its surface already adopted within `Morning Star` is employed, yielding a discrete representation of the surface of each array, which as said is assumed to follow the shape of the airship envelope. For each k-th discrete surface component, a normal unit vector $\boldsymbol{n}_k$ is obtained, with a corresponding known direction in space (i.e., resulting from the assumed position and orientation of the airship, dictated by the assigned mission profile and the wind at any time). The direct component of the solar irradiance for each discrete unit can be computed from the product

$$I_{b,k} = \begin{cases} G_b \boldsymbol{s}_{sun} \cdot \boldsymbol{n}_k, & \boldsymbol{s}_{sun} \cdot \boldsymbol{n}_k \geq 0, \\ 0, & \boldsymbol{s}_{sun} \cdot \boldsymbol{n}_k < 0 \end{cases} \tag{14}$$

where the condition in Eq. (14) means simply that the irradiance $I_{b,k}$ is null if the panel is not exposed to the Sun irradiance. The diffused component has been computed as a flow normal to the plane of the horizon. However, for its very nature (i.e., diffused), it is assumed to travel in an isotropic form, thus impacting the panel with the same estimated intensity G_{dh} whatever the direction $\boldsymbol{n}_k$ of the discrete panel unit, and correspondingly yielding an irradiance $I_{d,k} = G_{dh}$. Finally, $I_k = I_{b,k} + I_{d,k}$.

Table 2
Thermophysical properties of assumed solar cell layers.

Property	Symbol	Substrate [42], [43]	Cell layer [44], [45]	Encapsulation [46], [47]
Material		Kapton®	CIGS	Tefzel™
Thickness [mm]		0.025	0.002	0.025
Density [kg/m^3]		1420	5770	1700
Transmittance	τ	0.86	0	0.9
Absorbance	α	0.07	0.84	0.0458
Emissivity	ε	0.59	0.31	0.5
Thermal conductivity [W/(m K)]	K	0.20	3.7	0.24
Specific heat [J/(kg K)]	C_p	1090	300	1172

3.3. Solar cells modeling

Considering an ideal station-keeping mission, where the airship is kept for a time frame of days or months at the same position and altitude over the surface, the oscillation of the temperature on Mars on daily and seasonal time frames is such to change the characteristics of the solar array, considering in particular the photoelectric conversion efficiency, leading to potentially inaccurate predictions of the power balance on board when these effects are not considered. Therefore, to the aim of modeling the technological features of the arrays, which are functions of the temperature, the features of their components need a dedicated assessment. Despite their lower energy conversion efficiency compared to rigid, crystalline Silicon or Gallium arsenide cells, thin film solar cells based on amorphous Silicon (a-Si), Cadmium telluride (CdTe) and Copper Indium Gallium selenide (CIGS) technology have grown rapidly. In particular, CIGS cells can be produced on flexible substrates (polyimide or lightweight metals), making them moldable on curved solids like the envelope of an airship, and offer good radiation resistance, thus increasing durability in a thin atmosphere environment with intense radiation [40].

For this research, the properties of a cell similar to Ascent Solar CIGS [41], for which some data can be retrieved or reliably guessed, have been assumed. Three layers are considered in the CIGS cells. The substrate is a polyimide material layer 25 μm thick. It is here assumed to be Kapton® by DuPont™. For the external encapsulation layer, high-grade optical clarity materials with anti-reflective properties and environmental resilience are high-thermal plastics, like FEP, ETFE, TPU and polycarbonate. The characteristics of Tefzel™, a fluoropolymer film made by Teflon™, are considered. The properties assumed for the solar cells just described, employed in the airship sizing procedure, are reported in Table 2.

The photoelectric conversion efficiency can be assumed to be a linear function of the temperature, as in Eq. (15) [13],

$$\eta_{sc} = \eta_{sc,STD} \big(1 + \alpha_T (T_{sc} - T_{sc,STC})\big), \tag{15}$$

where subscript $(\cdot)_{STC}$ stands for standard testing conditions, and correspondingly from data sheets $\eta_{sc,STD} = 13\%$, $T_{sc,STC} = 25\,°\mathrm{C}$, and α_T = -0.0035 K^{-1} as typical for CIGS thin modules. Eq. (15) reflects a physical behavior, where the efficiency increases with a reduction of the temperature of the panel. However, this trend is physically arrested for a certain temperature $T_{\eta_{sc_{\max}}}$, which corresponds to a top value of the efficiency [48]. In the domain corresponding to values of the temperature below $T_{\eta_{sc_{\max}}}$, the linear model is mirrored by assumption, yielding the overall behavior reported in Fig. 3.

From Fig. 3, the value of $T_{\eta_{sc_{\max}}}$ for the technology of the solar cells selected in the present research is 150 K.

3.4. Thermal model of the envelope and solar cells

A major modification to the baseline methodology is closely related to the previous point (Section 3.3) and the need to define the evolution

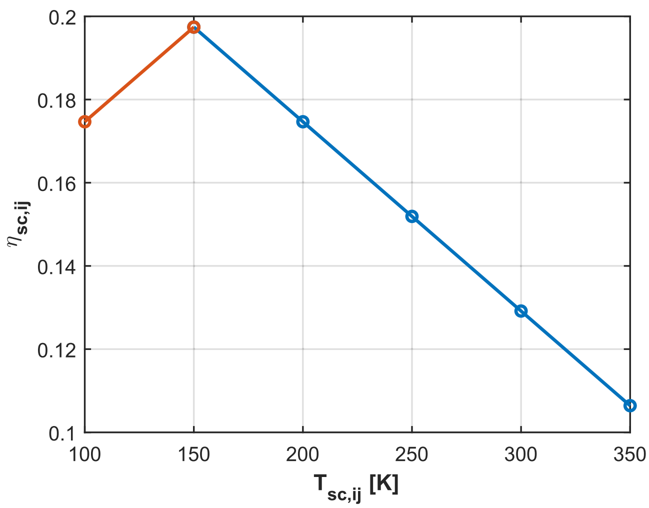

Fig. 3. Assumed variation of conversion efficiency of the solar cells with temperature.

of the temperature (primarily) of the thin solar cells on the airship, over a mission taking a time comparable to the period of the seasonal oscillation on Mars. Some consideration to the evolution of the temperature of the lifting gas within the envelope will be given here as well.

The topic has received limited attention in the literature, yet a baseline has been established by Alam and Pant [49,50], and developed independently as well by Zheng [51,52] and Hong [53], with different level of detail concerning the modeling of heat flows, but with the extension to the modeling of the temperature field on extended objects (e.g. the envelope). All these works consider invariably a terrestrial case. Proceeding within the framework proposed by Alam and Pant [49,50], a thermal model of the airship for the task can be set up according to a lumped parameters architecture. The thermodynamics are reduced to the oscillation of pressure and temperature, assuming no corresponding change to the volume or shape of the envelope. Furthermore, only the thermal properties of the envelope and the cells are considered, whereas other onboard components are neglected (e.g., the fins, motors). Finally, in that research, the environmental conditions are assumed constant over time. The latter hypothesis (i.e., a time-constant model) would be acceptable for short missions, but in this research this hypothesis is removed, thus enabling an analysis of the time evolution of temperature and lifting gas pressure over a long mission (e.g., a station-keeping mission potentially taking days or months).

The six nodes and thermal fluxes considered in the model adopted for this research are represented in the schematic view of Fig. 4, and their corresponding models will be synthetically reviewed here.

3.4.1. *Input solar irradiance fluxes*

The solar cells and envelope are reached by solar irradiance, and the corresponding fluxes are $\dot{Q}_{d_{sc}}$ and $\dot{Q}_{d_{env}}$ respectively. For the k-th discrete component of the surface of either the cells or the envelope, an elemental flux can be computed on account of the mutual orientation of the incoming beam and the surface. The sum of all these contributions produces the overall flux. In analytic terms, these fluxes can be assigned as

$$\begin{aligned} \dot{Q}_{d_{sc}} &= \sum_k (1-\eta_{sc})\alpha_{sc} I_k A_{sc,k}, \\ \dot{Q}_{d_{env}} &= \sum_k \alpha_{f,eff} I_k A_{env,k}. \end{aligned} \tag{16}$$

For solar cells, it is assumed that the absorbance coefficient α_{sc} is that of the solar CIGS layer only, on account of the high value of transmittance of the external encapsulation layer (see Table 2). Notably, the photoelectric efficiency η_{sc} is a function of the temperature as per Eq. (15).

For the envelope, the value of the effective absorbance $\alpha_{f,eff}$ has been computed according to Eq. (17) [54],

$$\alpha_{f,eff} = \alpha_f \left(1 + \frac{\tau_{f,sol}}{1 - r_{f,sol}}\right), \tag{17}$$

where parameters $\tau_{f,sol}$ and $r_{f,sol}$ are the spectrum transmittance and reflectance of the external coating layer of the envelope material, typically deployed specifically for reducing the flux penetrating to the inner load-bearing layers of the envelope material. ■

3.4.2. *Irradiance flux with the environment*

The top layer of the solar cells and the envelope exchange (typically emit) an irradiance flux with the atmospheric environment, according to Boltzmann's equations

$$\begin{aligned} \dot{Q}_{IR_{glass}} &= \varepsilon_{glass} A_{glass} \sigma (T_{bb}^4 - T_{glass}^4), \\ \dot{Q}_{IR_{env}} &= \varepsilon_{f,env} A_{env} \sigma (T_{bb}^4 - T_{env}^4), \end{aligned} \tag{18}$$

where σ is Boltzmann's constant, ε_{glass} is the emissivity of the encapsulation element of the solar cells (see Table 2), $\varepsilon_{f,env}$ is the effective emissivity of the envelope, computed from Eq. (19) [54], formally similar to Eq. (17), yielding

$$\varepsilon_{f,eff} = \varepsilon_f \left(1 + \frac{\tau_f}{1 - r_f}\right), \tag{19}$$

where τ_f and r_f are the full spectrum transmittance and reflectance of the envelope external coating layer. The black globe temperature of the environment T_{bb} can be estimated to 60% of the environment (i.e., atmospheric) temperature T_{atm} [48]. ■

3.4.3. *Irradiance flux within the airship layers*

Referring to Fig. 4, the fluxes $\dot{Q}_{IR_{gas\to bsc}}$ and $\dot{Q}_{IR_{gas\to env}}$ are assumed null, on account of the transparency of the lifting gas (either Hydrogen or Helium) to the irradiative transfer. Conversely, the irradiance flux between the envelope portion under the solar cells and the envelope can be accounted for according to Boltzmann's law,

$$\dot{Q}_{IR_{bsc\to env}} = \varepsilon_{f,eff} A_{bsc} F_{bsc\to env} \sigma (T_{bsc}^4 - T_{env}^4), \tag{20}$$

wherein T_{bsc} is the temperature of the envelope component underneath the solar cells, and the view factor $F_{bsc\to env} \simeq 1$, on account of the specific mutual positioning and difference in sizing (i.e., $A_{bsc} << A_{env}$), of the two elements. ■

3.4.4. *Convection fluxes with the environment*

Convection fluxes are exchanged at the level of the coating of the solar cells and of the external surface of the envelope, due to the presence of a generally non-negligible airspeed, induced by the wind even for a station-keeping mission. The corresponding respective expressions are reported in Eq. (21), yielding

$$\begin{aligned} \dot{Q}_{CV_{atm\to glass}} &= h_{ext} A_{glass} (T_{atm} - T_{glass}), \\ \dot{Q}_{CV_{atm\to env}} &= h_{ext} A_{env} (T_{atm} - T_{env}). \end{aligned} \tag{21}$$

An estimation of the convective heat transfer coefficient h_{ext} for the present case can be obtained as [49]

$$h_{ext} = \frac{Nu \cdot K_{atm}}{D_{\max}}, \tag{22}$$

where K_{atm} represents the conductivity of the atmosphere, and can be estimated through a linear law with respect to the ambient temperature considering the conductivity of Carbon dioxide as dominant within the Martian atmosphere [55], thus yielding $K_{atm} = -0.0070 + 0.0001 T_{atm}$. The Nusselt number Nu is estimated with the regression prepared for a spherical balloon by Farley [56], yielding $Nu = 2.00 + 0.41 Re^{0.55}$. The accuracy of this estimation is supported *a posteriori* on account of the relatively low fineness ratio f featured in the sizing solutions (see Section 4). ■

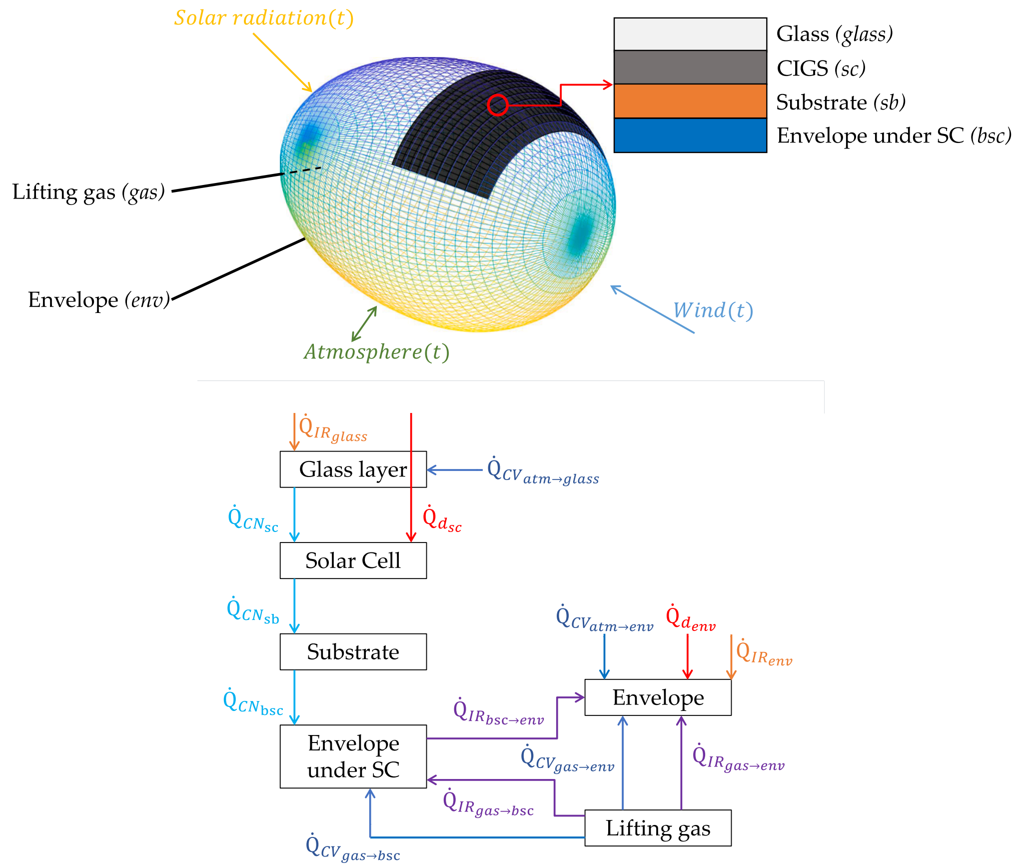

Fig. 4. Thermal model representation. Top: three-dimensional representation of envelope and solar panels. Bottom: identity of nodes, fluxes and connections.

3.4.5. *Convection fluxes within the airship components*

The lifting gas exchanges convective fluxes with the envelope and with the component of the envelope beneath the solar cells. The corresponding heat fluxes are modeled as in Eq. (23), yielding

$$\begin{aligned}\dot{Q}_{CV_{gas\to env}} &= h_{in}A_{env}(T_{gas}-T_{env}),\\ \dot{Q}_{CV_{gas\to bsc}} &= h_{in}A_{bsc}(T_{gas}-T_{bsc}).\end{aligned} \tag{23}$$

An estimation for the convective heat transfer coefficient h_{in} can be provided assuming the identity of the lifting gas (or mixture) [57]. Its expression yields

$$h_{in} = 0.13\frac{K_{gas}}{D_{\max}}(Gr\cdot Pr)^{\frac{1}{3}} \tag{24}$$

and is a function of the thermal conductivity K_{gas}, Grashof and Prandtl numbers Gr and Pr. The conductivity can be estimated through a linear relationship with the lifting gas temperature T_{gas}, yielding for Hydrogen $K_{gas} = 0.0192 + 0.0005\cdot T_{gas}$ [55]. The Prandtl number is defined as $Pr = \frac{C_{P,gas}\mu_{gas}}{K_{gas}}$, where the isobaric specific heat and dynamic viscosity of the lifting gas can be modeled as linear functions of the temperature T_{gas} (e.g., for Hydrogen $C_{P,gas} = 11{,}619.7 + 9.348\cdot T_{gas}$ and $\mu_{gas} = 10^{-6}(2.3696 + 0.0217T_{gas})$). Finally, the Grashof number is defined as $Gr = \frac{g\beta|T_{(\cdot)}-T_{gas}|D^3_{\max}}{\nu^2_{gas}}$, where ν_{gas} is the kinematic viscosity of the lifting gas, obtained from the dynamic viscosity under hypothesis of constant volume, g is Mars gravity, $\beta \simeq \frac{1}{T_{gas}}$ is the volumetric thermal expansion coefficient (estimation valid for an ideal gas), and $T_{(\cdot)}$ represents the temperature of either the envelope or the portion of the envelope under the solar cells. ■

3.4.6. *Conductive fluxes*

Conductive fluxes appear within the layers of the solar cells, as well as the portion of the envelope underneath the cells. The three fluxes in Fig. 4 bear formally similar expressions, yielding

$$\begin{aligned}&\dot{Q}_{CN_{sc}} = \frac{A_{sc}(T_{glass}-T_{sc})}{\frac{d_{glass}}{K_{glass}}+\frac{d_{sc}}{K_{sc}}},\quad \dot{Q}_{CN_{sb}} = \frac{A_{sb}(T_{sc}-T_{sb})}{\frac{d_{sc}}{K_{sc}}+\frac{d_{sb}}{K_{sb}}},\\ &\dot{Q}_{CN_{bsc}} = \frac{A_{bsc}(T_{sb}-T_{bsc})}{\frac{d_{sb}}{K_{sb}}+\frac{d_{bsc}}{K_{bsc}}}.\end{aligned} \tag{25}$$

In Eq. (25), $K_{(\cdot)}$ and $d_{(\cdot)}$ are conductivity and thickness values for the respective layers, listed in Table 2 for solar cells, or obtained from data sheets corresponding to the selected envelope material. ■

All fluxes just modeled contribute to the setup of a dynamic model for the temperature of the nodes in the adopted architecture (Fig. 4). The energy balance equations for the six nodes in the model can be written as follows:

$$\text{Solar cells}\begin{cases} m_{glass} C_{P_{glass}} \dfrac{dT_{glass}}{dt} = \dot{Q}_{IR_{glass}} - \dot{Q}_{CN_{sc}} \\ \qquad + \dot{Q}_{CV_{atm \to glass}} \\ m_{sc} C_{P_{sc}} \dfrac{dT_{sc}}{dt} = \dot{Q}_{d_{sc}} + \dot{Q}_{CN_{sc}} - \dot{Q}_{CN_{sb}} \\ m_{sb} C_{P_{sb}} \dfrac{dT_{sb}}{dt} = \dot{Q}_{CN_{sb}} - \dot{Q}_{CN_{bsc}} \end{cases}$$

$$\text{Envelope}\begin{cases} m_{env} C_{P_{env}} \dfrac{dT_{env}}{dt} = \dot{Q}_{d_{env}} + \dot{Q}_{CV_{atm \to env}} + \dot{Q}_{CV_{gas \to env}} \\ \qquad + \dot{Q}_{IR_{env}} + \dot{Q}_{IR_{bsc \to env}} \\ m_{bsc} C_{P_{bsc}} \dfrac{dT_{bsc}}{dt} = \dot{Q}_{CN_{bsc}} + \dot{Q}_{CV_{gas \to bsc}} - \dot{Q}_{IR_{bsc \to env}} \end{cases} \tag{26}$$

$$\text{Lifting gas}\left\{ m_{gas} C_{V_{gas}} \dfrac{dT_{gas}}{dt} = -\dot{Q}_{CV_{gas \to bsc}} - Q_{CV_{gas \to env}} \right.$$

In Eq. (26) the specific heat capacity of the layers of the solar cells ($C_{P_{glass}}$, $C_{P_{sc}}$, $C_{P_{sb}}$) can be obtained for the cell technology adopted here from Table 2, whereas the specific heat capacity of the envelope $C_{P_{env}}$ can be obtained from its own conductivity for a specific material. Finally, the isochoric specific heat capacity of the lifting gas $C_{V_{gas}}$ is computed with Mayer's law from the corresponding isobaric value, when the gas constant R_{gas} for that gas is known, yielding $C_{V_{gas}} = C_{P_{gas}} - R_{gas}$.

As just shown, most characteristics contributing to the thermal model are functions of the temperature, making the system in Eq. (26) a time-variant one. Furthermore, it should be recalled that the need for a thermal model for the airship is here implied by sizing purposes, primarily in order to enable an accurate sizing of the masses of all components. The inclusion of the thermal model in the sizing procedure is as follows. An additional layer of iteration is implemented. The sizing loop (see Section 2.1.1) is run in a first iteration with guess values of the technological properties of the solar panels and envelope, with no thermal analysis. This first-iteration sizing allows to compute the masses of all components, in particular, populating the mass coefficients in the thermal nodes of Eq. (26). The mass of the solar panels being known as a total value, the respective shares of the encapsulation, solar cells and substrate are assigned based on the respective percent thickness within the solar panel, which are assumed as constant parameters from Table 2 (similar to the case of the envelope). Then, starting from a user's defined initial time, date and location of the mission (e.g. midnight at an assigned solar longitude, at specific coordinates over the surface of Mars), the thermal analysis is carried out by solving Eq. (26) over the time frame of the mission, obtaining the evolution of the temperature. Numerically, this integration is performed on a discrete time domain, considering a baseline time step of one hour, with a multi-step integration scheme for stiff systems, without reported relevant issues (see Section 4.3). The time profile of the temperature is employed to compute the time evolution of the technological features of the panels, in particular the photoelectric efficiency, over the mission time span. This enables running a new iteration in mass sizing, thus triggering an inner iterative process until convergence, actually making the sizing loop an iterative procedure of its own. The optimum-seeking algorithm remains untouched, steering the solution towards overall mass-optimality and imposing compliance with the constraints (see Section 2.1.2).

As anticipated, the thermal model envisaged herein allows to accurately compute the temperature of the lifting gas. In particular, the excursion of the temperature is relevant for sizing, and is such to yield also a corresponding evolution of the inner pressure over the mission profile. In the original sizing procedure [13,15], lacking a dynamic thermal model of the airship, this excursion in the lifting gas temperature was assumed equal to the change in the ambient temperature. Some testing was carried out in this research, sizing an airship for a specific position and altitude on Mars (86.0°N, 180.0°E, 2,000 m altitude) and for a one-day mission, repeating the sizing for a solar longitude L_s between 0° and 180°, corresponding to the season free of dust storms and most interesting for atmospheric flight [22]. When computing the evolution of T_{gas} for each sizing and comparing it to the corresponding evolution of the ambient temperature, the average of the instantaneous gap $\max_t(T_{atm}(t) - T_{gas}(t))$ reported in Fig. 5 was obtained.

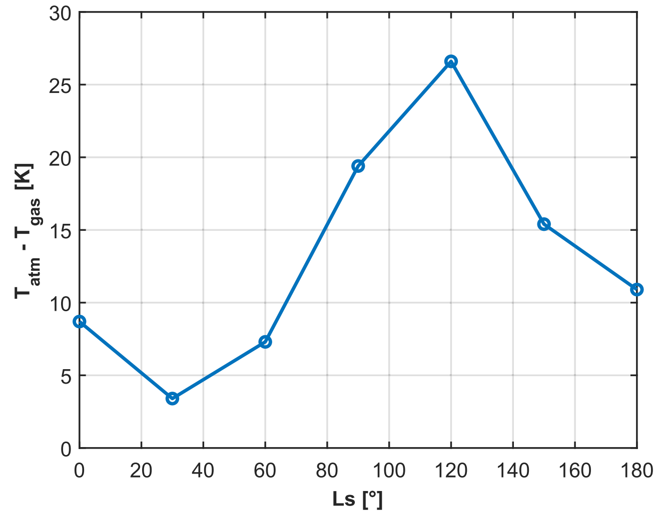

Fig. 5. Daily-averaged difference between the temperature of the atmosphere T_{atm} and of the lifting gas T_{gas}, as a function of the solar longitude L_s.

Where a gap is of course present, its relative value compared to the absolute temperature T_{atm} for that solar longitude L_s has been evaluated at 13% in the worst case. Therefore, the inaccuracy resulting from assuming no difference between the ambient and lifting gas temperature is likely justified, and the approach implemented in the original `Morning Star` suite with regard to the lifting gas temperature has been retained.

3.5. Model for the propulsion system

The methodology originally adopted in `Morning Star` for the mass and power sizing of the propulsion system is changed in some aspects, mainly due to a different approach in the mass prediction. The latter was originally based on a model linking the complete electric motor mass to the maximum shaft power, and had a validity range of roughly 1 to 100 kW. However, given the extremely low density of the Martian atmosphere, the resulting maximum shaft power is considerably low, usually in the range of hundreds of Watts. For this reason, a new model is implemented, more suitable to this low power conditions. The model proposed by Colozza in his work "Airships for Planetary Exploration" [18] is adopted, which calculates the mass of the electric motor group (i.e. electric motor, gearbox and control electronics) based on a linear scaling with the power output, and with a correction for low power cases. In order to evaluate the power required, the function needs as input some characteristic efficiencies, namely the electric motor efficiency η_m, the gear transmission efficiency η_g, and the propeller efficiency η_{prop}. The first two are directly taken from the default settings as equal to 0.9 ad 0.97 respectively; whereas the latter is initially taken as equal to an optimistic 0.8, but it's the topic of the analysis reported in Section 4.4.4.

Finally, the mass of the propellers is computed using the same mass-to-power ratio considered in the original methodology (i.e. 0.5 kg/kW) [13,14]. This, as will be shown in Section 4.4.2 Table 7, will lead to quite low propellers masses, especially when compared to typical values in the aeronautical field, with results ranging from about 0.03 kg to 0.2 kg for one propeller (i.e. $m_{prop}/4$). However, more refined and lightweight technologies would be involved in the actual structural sizing of the present case than what is of common use for aeronautical propellers on Earth, as demonstrated by the design of rotors for Martian use (both past and under development) [58,59]. The Ingenuity helicopter for instance had a rotor diameter of 1.21 m and blades of just 28 g each. Considering a geometrical scaling factor with the airship propellers of 1.65 (i.e. the ratio between the diameters of the airship propeller developed here and the Ingenuity rotor), and assuming that the mass would grow with the third power of it, the resulting airship propellers are expected to have a mass of around 0.25 kg each. Proceeding in the same way with the Mars Science Helicopter (MSH), currently under development, and featuring a blade mass of 71.3 g, the scaling factor would be 1.56, resulting in an expected propeller mass of 0.55 kg. Moreover, it should be noted that the rotors taken as examples are typically subjected to higher aerodynamic and inertial loading, induced by greater tip speeds and higher spinning rate. These considerations, although of basic accuracy, support that the mass considered for the propellers in the present study is within range of what should be expected, and possible variations with respect to the results presented above from the sizing methodology would increase their contribution to the overall mass budget of the airship of just hundreds of grams (a level of precision exceeding the general accuracy level of the preliminary sizing phase at hand).

4. Mission settings and parameterized sizing results

The sizing methodology described in the previous sections has been employed to assess the feasibility and bottlenecks of the design of an airship for a mission on Mars. In the next paragraphs, after introducing some assigned settings defining a candidate mission, and some relevant fixed technological parameters, a parameterized analysis showing the effect of some relevant technical choices in determining the sizing solution will be presented, thus highlighting the drivers and the obstacles to the feasibility of an airship solution for the mission at hand.

4.1. Candidate mission

As mentioned in the introduction (Section 1.3), the exploration of Mars via atmospheric flight has some features matching the ability of an airship platform. Among the most interesting areas of the planet, the northern polar region and specifically the Mars Transverse Mercator MTM 85200 offers locations where the upper stratigraphic sequences of the North Polar Layered Deposits (NPLD) are potentially accessible [60], allowing an in-depth study of the past climate of Mars and the very formation of NPLD. However, the extremely uneven terrain morphology, with scarps up to 500 m in depth like in the Olympia Rupes region, *de facto* hamper exploration by land rovers. On the other hand, the need to scan the soil with deep-penetrating radar sounds, requires a payload capacity superior to that offered by rotary wing technology, and a similar ability to hover.

In this scenario, a station-keeping mission is envisaged, specifically picking coordinates 86,0°N, 180.0°E, lying within MTM 85200, and adopted as an example for data sourcing on atmospheric and irradiance quantities. A stationing altitude of 2,000 m is selected, such to grant the ability to employ the airship over the rugged morphology of the nearby region, where high-gradient changes of the terrain elevation of up to 1,000 m are featured. The solar longitude span considered for the mission is only between $L_s = 0°$ and 180°, which exclude the time frame of dust storms (Mars winter), and in the selected location (i.e., near the north pole) offers an intense irradiance level, extending in the summer to the entire duration of a daily rotation (midnight Sun) [22]. This selection tackles one of the limiting factors in the analysis by Colozza [18], while implicitly showing (as observed on Earth as well [14]) that the sizing of an airship operating as a station-keeping platform on a time frame of days or months is strongly dependent on the coordinates on the surface, due to the different intensity and direction of irradiance experienced over time at that location.

Concerning the duration of the mission, the target is that of covering the time frame corresponding to the orbital travel of Mars between the selected solar longitudes (corresponding to 382.12 Earth days). For the terrestrial case, the implementation of `Morning Star` allows to carry out the sizing for an yearly mission considering at first the most energetically requiring day cycle (i.e., the full 24 h time frame) of the year, then testing the corresponding sizing on all other days, checking the compliance with respect to weight support, energy sustainability and stress integrity in any condition (see Section 2.1.2). The same strategy can be applied for Mars, considering instead of a yearly mission, one which extends between the solar longitude values just mentioned. However, for better appreciating the effect of the change in the environmental conditions resulting from a different solar longitude, the results presented within the parameterized analysis will show the sizing solutions corresponding to one-day missions (mid-night to mid-night), considering not just the most demanding day (corresponding to a specific longitude $L_s = L_s^*$), but also other values of L_s.

It is worth mentioning that, concerning the irradiance model (Section 3.2), the choice of the solar longitudes for the mission allows to define an average value of the optical depth of the atmosphere at ground level from the data collected by the Viking lander [36]. For L_s between 0° and 180°, an assumed constant value of $\tau_0 = 0.46$ is well representative of the actual behavior of this parameter over time.

Concerning the payload, where a detailed break-down is not needed for preliminary sizing, credible values for the weight and required power values for the mission just introduced shall be assumed. Colozza [18] cites a weight of 20 kg and a power of 50 W, whereas Pozhanka and Hassanalian assume 25 kg and 500 W [29]. The VALENTInE project, which analyzes the payload in much detail [20] despite on a mission significantly different from the one at hand, mentions 20 kg, with the a peak power, due to the infrared spectrometer, set to 20 W. For conservativeness, a baseline of 20 kg and 100 W is assumed, which is made more stringent as suggested by Colozza [18] on account of possible non-core electronic components, yielding $W_{pl} = 30$ kg and $P_{pl} = 200$ W for the next baseline computations.

To conclude with the mission assignment, it should be pointed out that the focus has been placed on the design of the airship, and not on the design of the Earth to Mars transfer of the components. Indeed, totally unrealistic mass and geometrical sizing of the components have been avoided in the settings and preliminarily checked *a posteriori* within the solution, as will be detailed in the next analysis. However, no hard constraint on either top geometry or mass values has been specified within the sizing algorithm.

4.2. Technology assumptions

Of particular relevance for the sizing procedure are the characteristics of the lifting gas, the envelope, the solar cells and the batteries. The selected lifting gas is pure Hydrogen, which offers the best characteristics in terms of net buoyancy for an assigned volume, being the lightest gas. It is commonly employed for Earth applications [4,5], and the Martian atmosphere, composed of Carbon-dioxide, mitigates the risk of accidental combustion phenomena. The airship, just like in the baseline implementation [13], is designed as a super-pressure non-rigid platform. In this architecture, the volume of the envelope is fixed, and when the temperature of the lifting gas is the coldest, the pressure differential with the atmosphere is such to ensure shape preservation, and sufficient rigidity to avoid caving [61]. For a higher inside temperature (hence pressure), the differential pressure is increased. By estimating the maximum superpressure, from maximum super-heat, it is possible to estimate the maximum stress that the envelope needs to sustain, and based on the structural resistance of the adopted material, this produces a corresponding sizing to guarantee integrity [13]. To assign the minimum pressure differential for shape preservation in presence of dynamic pressure (i.e., to avoid caving in presence of an airspeed), a pressure difference value is computed based on regulations in the original procedure for Earth ap-

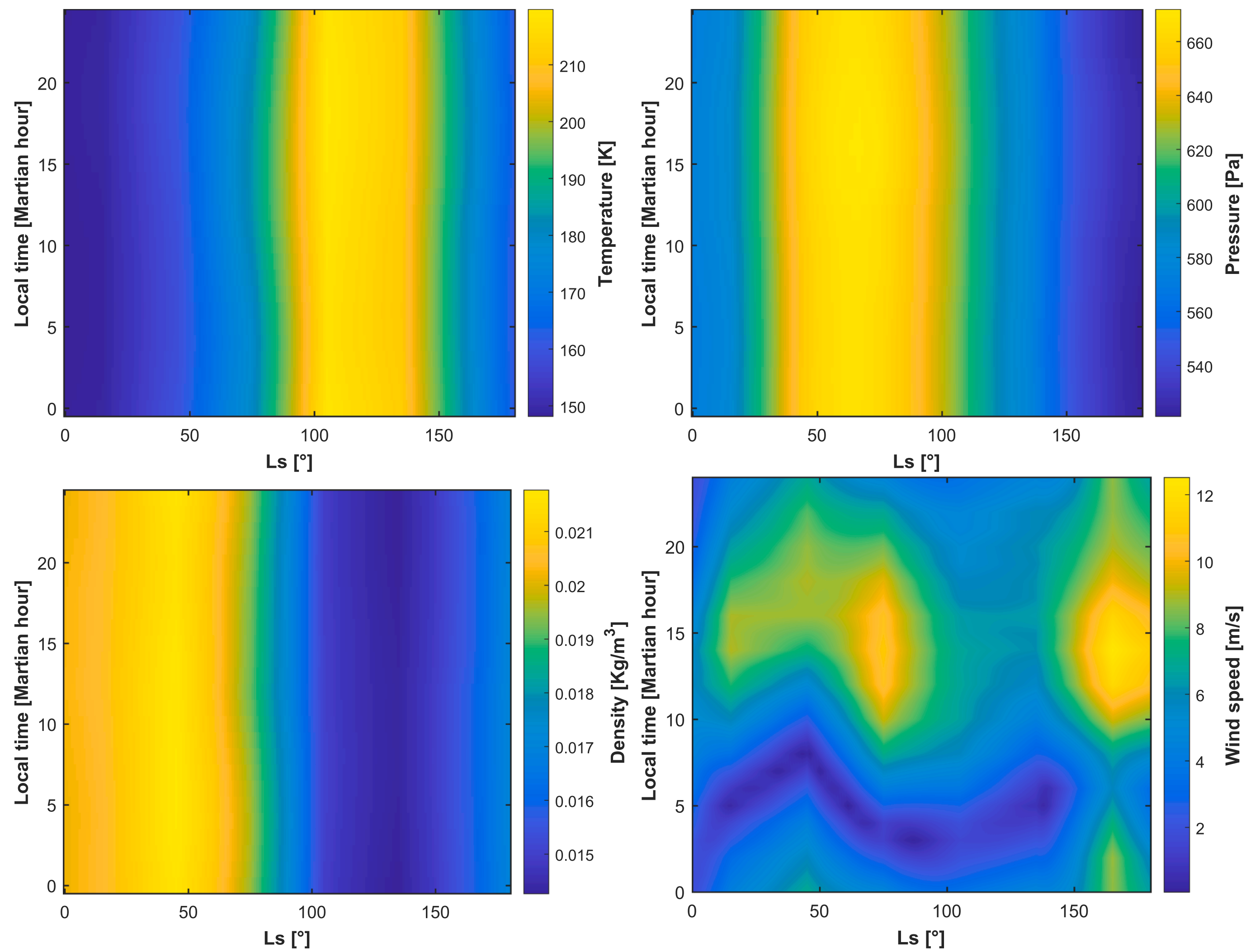

Fig. 6. Physical properties of the Martian atmosphere generated by MCD v6.1 [30] with climatology average solar scenario for the selected mission position and altitude, as functions of the time of the day and solar longitude. Top left and right: temperature and pressure. Bottom left and right: density and horizontal wind intensity.

plications. In this case, hypothesizing a zero ground speed, the value of the top wind encountered over the mission profile has been employed to compute such pressure difference, once increased by a safety margin of 30% accounting for gusts (see Fig. 6). The maximum super-heat, i.e. the top increase of T_{gas} with respect to the minimum over the mission profile, is obtained interrogating the atmospheric model MCD [30] for the location and date/time of interest, and it can be estimated at 72 K for the overall time of the mission (Fig. 6).

Some top-tier materials employed for airship and balloons have been considered for the envelope, including para-aramids (Kevlar®), ultra-high molecular weight polyethylene (UHMWPE, like Spectra® and Dyneema®), polyarylate (Vectran®) and PBO (Zylon®), covering a wide range of density and breaking strength values [61]. Vectran® [62] laminated fabric has been selected for the mission, firstly on account of its excellent creep and abrasion resistance, durability under flexing and folding, and performance-keeping (including a generally low thermal expansion) across a wide range of temperatures. In a scenario where patching and fixing are extremely difficult, and in view of needed folding for transfer to the deployment point, the resilience of the envelope has been deemed crucial, similar to the low sensitivity to atmospheric conditions, even though the strength of this material is lower than for PBO or UHMWPE based solutions. Within `Morning Star`, a regressive curve returning area density from the breaking strength for this material is employed [13], allowing to link the computed pressure differential and related stress to the density, which in turn is employed to compute the mass of the envelope from the volume and surface available from previous passages in the sizing loop. Before entering the computation of the density from the critical stress however, a safety factor of 4.0 is employed within `Morning Star` to increase the stress value obtained from the previous estimation just outlined. This safety factor will be considered as a tunable parameter in the next parameterized analysis.

Considering the thermal characteristics of the envelope material, Vectran® takes the structural load bearing and gas keeping features, and it can be wrapped in a polyethylene film coating [54] for better irradiance protection. The features of the film coating, as mentioned in 3.4, influence the thermal model of the envelope. The assumed characteristics of this film are reported in Table 3, as needed for Eqs. (17) and (19).

Additionally, the thermal conductivity of Vectran® has been assumed equal to $K_{bsc} = 1.5$ W/m K, and its specific heat capacity $C_{P_{env}} = C_{P_{bsc}} = 1{,}100$ J/(kgK) [63].

Concerning the solar cells, the technological features described in Section 3.3 have been adopted, thus amending the original procedure, in conjunction with the dynamic thermal modeling shown in Section 3.4.

Concerning the batteries, the default values of technological parameters employed within `Morning Star` are adopted [13],

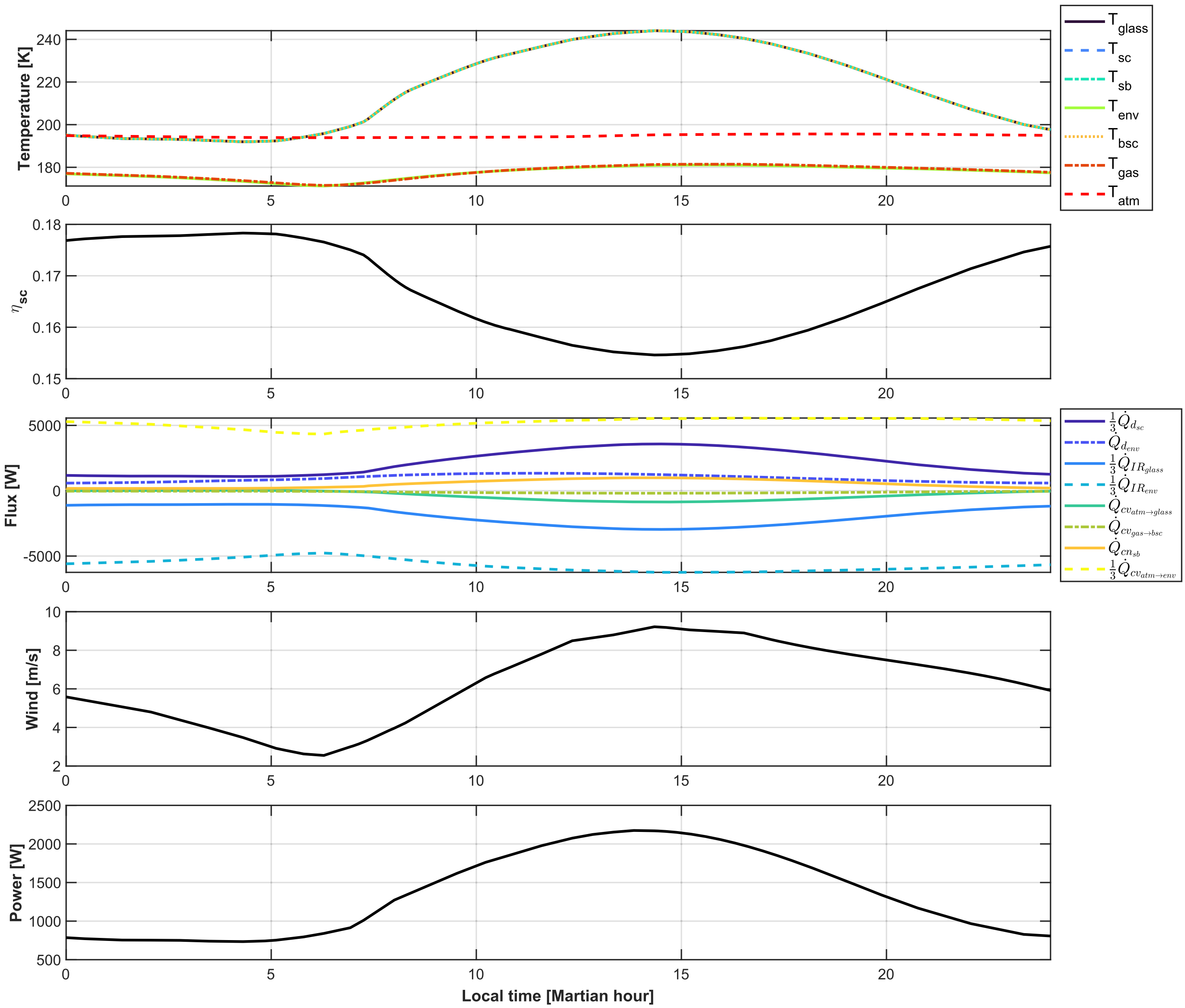

Fig. 7. Outcome of the thermal model for an example airship sizing, for $L_s = 150°$. From top to bottom: temperature of the nodes, photoelectric conversion efficiency of the solar cells, fluxes (some down-scaled to 1/3), wind intensity, power available from the solar array.

Table 3
Assumed optical parameters of film coating for irradiance protection.

Parameters	Symbol	Value
Absorbance	α_f	0.001
Emissivity	ε_f	0.031
Transmittance	τ_f	0.842
Transmittance (solar)	$\tau_{f,sol}$	0.885
Reflectance	r_f	0.127
Reflectance (solar)	$r_{f,sol}$	0.114

corresponding to Li-ion chemistry. The latter has been considered conservative compared to Li-S and Li-metal options, which offer better power and energy density at the price of worse stability characteristics and a reduced number of cycles. In particular, charge/discharge efficiency has been set to 0.96, the depth of discharge to 0.95, and the mass-specific and volume-specific energy densities to e_{bat} = 900 kJ/kg and ρ_{bat} = 2,052 MJ/m^3.

4.3. Example results of the thermal analysis

To show the thermal model at work and provide an impression of the relevance of the corresponding temperature oscillations, two examples are shown in Figs. 7 and 8, pertaining to two different solar longitude values L_s.

In these examples, for a representative airship with L = 60 m and f = 1.5, an area of the solar cells A_{sc} = 93 m^2, at the design location and altitude introduced previously, the figures report (from top to bottom) the temperature of the six nodes in the model, the conversion efficiency η_{sc} of the solar array, notable thermal fluxes, and the power available from the solar array. Fig. 7 refers to a solar longitude $L_s = 150°$ and Fig. 8 to $L_s = 180°$. Notably, fluxes $\dot{Q}_{d_{sc}}$, $\dot{Q}_{IR_{glass}}$, $\dot{Q}_{IR_{env}}$ and $\dot{Q}_{CV_{atm\to env}}$ have been down-scaled to 1/3 of their value purely for graphical purposes, to better compare their time behavior with other fluxes.

Looking at both figures, it can be noted that the temperatures related to the three components of the solar array and to the portion of the envelope beneath the solar panels (namely T_{glass}, T_{sc}, T_{sb} and T_{bsc}) are basically indistinguishable, as expected, since these components are very closely packed. Their temperature is driven mostly by solar irradiance.

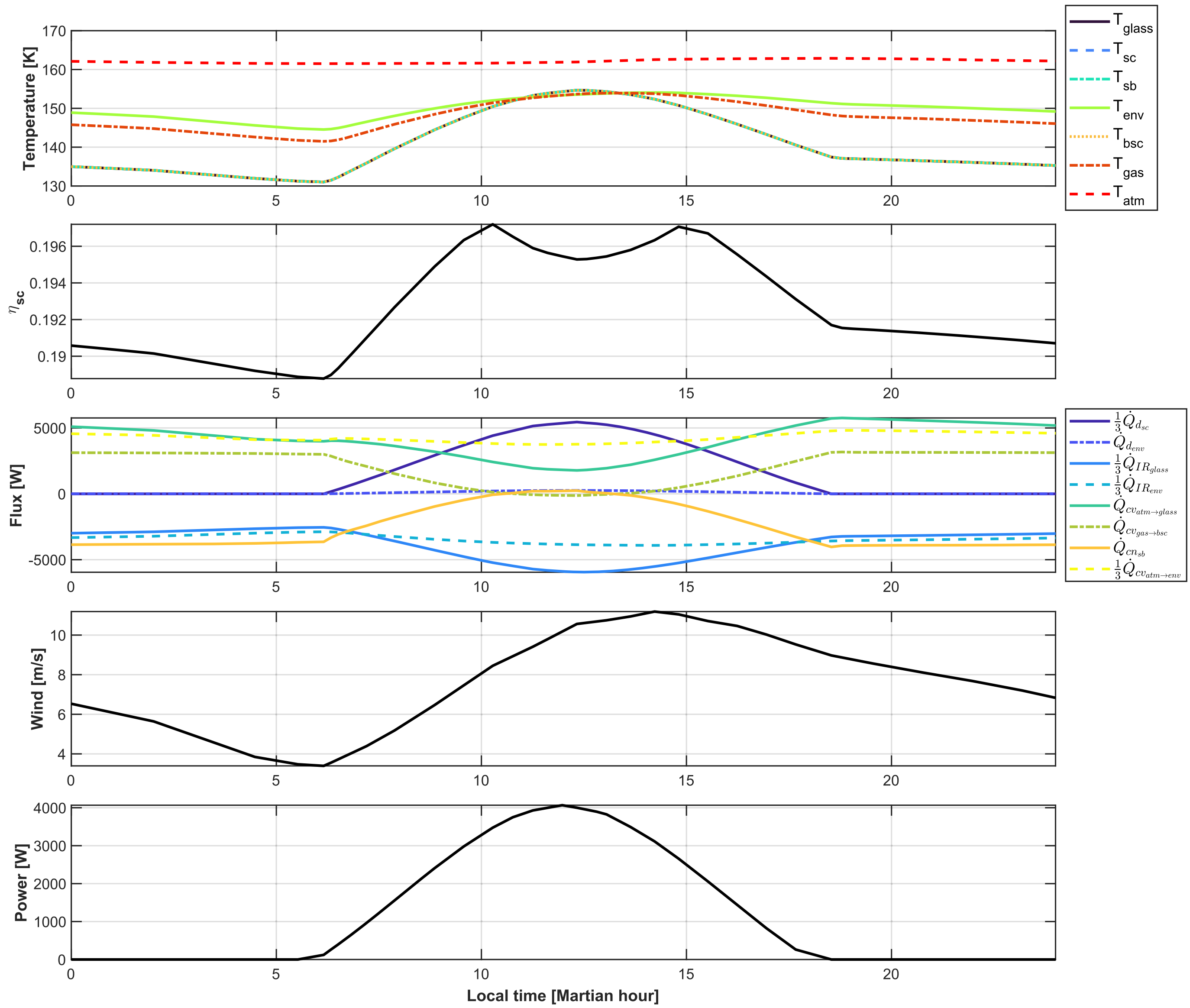

Fig. 8. Outcome of the thermal model for an example airship sizing, for $L_s = 180°$. From top to bottom: temperature of the nodes, photoelectric conversion efficiency of the solar cells, fluxes (some down-scaled to 1/3), wind intensity, power available from the solar array.

Over time, they show a visible correlation with the latter, i.e. with $\dot{Q}_{d_{sc}}$, which is clearly a major power flow and driver in the system. On the other hand, the system radiates intensely towards the atmosphere (see $\dot{Q}_{IR_{glass}}$ and $\dot{Q}_{IR_{end}}$), and temperatures are keeping within a relatively limited range. The temperature of the lifting gas T_{gas} closely follows that of the envelope T_{env}. Stark differences are encountered in the values of the convective fluxes between the two examples, which in the $L_s = 180°$ case warm up the solar cells, which never reach a temperature so high as the ambient one, whereas the opposite happens in the $L_s = 150°$ case. Most notably however, the photoelectric conversion efficiency of the arrays varies greatly over the day for both considered cases, as well as in terms of excursion comparing one case to the other. This further justifies the deployment of the thermal analysis as a means for attaining a good accuracy in the airship sizing, such to account for realistic values of the solar array efficiency at any time.

4.4. Parameterized analysis and trade studies

A baseline solution for the sizing has been obtained for allowing comparisons. Notably, in this baseline condition no ballonet system has been included, and the efficiency of the propeller has been assumed as typical to a terrestrial value, similar to the original `Morning Star` implementation ($\eta_P = 0.8$). The sizing has been carried out for a one-day mission, for different values of the solar longitude L_s between the extremes introduced above (Section 4.1). The parameters of the mass-optimal sizing for each of the considered solar longitudes are reported in Table 4, and the corresponding overall mass m, required energy storage E_{bat} (i.e., in the batteries) and envelope breaking strength σ_{lim} are reported as well.

As a general comment, the overall geometrical sizing (L, f and the solar cells sizing) is intensely changing with the solar longitude. Also the mass is changing significantly. The mass m is peaking for $L_s = 120°$, with a minimum at $L_s = 30°$ at a value below the 20% of the top. Interestingly, larger battery energy, required for instance at $L_s = 0°$ and $L_s = 180°$ does not come together with the highest weights, showing that the energy storage for an electric airship is not a significant driver for the overall mass (as already shown in the terrestrial case [7], and in stark contrast with fixed-wing applications of electric powertrains [64]).

Table 4
Baseline sizing solution for a one-day mission, for different L_s.

L_s [°]	L [m]	f [-]	x_{le} [m]	x_{te} [m]	θ_{in} [rad]	θ_{out} [rad]	m [kg]	E_{bat} [kWh]	σ_{lim} [N/cm]
0	69.5	2.02	7.6	40.6	1.20	2.15	865	4.23	193.5
30	55.7	1.76	5.0	18.0	0.50	0.89	606	0.34	191.3
60	62.0	1.84	5.0	8.8	0.50	1.34	762	0.40	221.6
90	95.7	2.08	5.0	10.5	0.50	1.00	1829	0.08	294.0
120	168.0	2.60	5.0	10.0	0.50	0.90	5348	0.00	381.5
150	116.5	2.15	5.0	27.2	0.50	0.74	2653	0.00	293.3
180	127.8	2.87	5.0	49.5	1.97	4.10	2264	16.1	229.9

Table 5
Baseline sizing solution in the same condition as Table 4, but null payload mass and power.

L_s [°]	L [m]	f [-]	x_{le} [m]	x_{te} [m]	θ_{in} [rad]	θ_{out} [rad]	m [kg]	E_{bat} [kWh]	σ_{lim} [N/cm]
0	64.0	2.02	7.6	40.6	1.20	1.90	675	2.31	178.2
30	53.7	1.88	5.9	18.0	0.50	0.89	483	0.00	173.9
60	57.3	1.84	5.0	8.80	0.50	1.33	604	0.00	204.7
90	91.8	2.08	5.0	10.5	0.55	1.00	1616	0.11	281.9
120	162.8	2.55	6.4	8.04	0.50	1.86	5038	0.00	376.1
150	113.2	2.15	5.0	27.2	0.50	0.73	2433	0.00	284.8
180	124.5	2.87	5.0	49.5	1.97	4.10	2093	13.4	223.9

Table 6
Sizing solution in the same condition as Table 4, but a safety margin of 2.0 on the envelope material (instead of 4.0).

L_s [°]	L [m]	f [-]	x_{le} [m]	x_{te} [m]	θ_{in} [rad]	θ_{out} [rad]	m [kg]	E_{bat} [kWh]	σ_{lim} [N/cm]
0	50.8	1.70	5.0	11.3	0.50	6.28	480	4.17	84.2
30	39.1	1.48	5.0	8.41	0.50	2.09	301	0.00	80.4
60	40.4	1.48	5.0	7.92	0.50	1.68	324	0.00	89.2
90	49.0	1.46	5.0	8.55	0.50	1.27	495	0.00	106.5
120	58.5	1.42	5.0	6.44	0.50	1.53	751	0.00	120.6
135	59.1	1.42	5.0	6.37	0.50	2.04	762	0.00	117.9
150	57.6	1.50	5.0	8.20	0.50	2.19	656	0.00	103.4
180	92.6	2.63	5.0	42.7	1.90	4.08	1020	11.6	90.4

4.4.1. Effect of payload

On account of the approximate forecast of the payload characteristics, just outlined, the same analysis as in the previous paragraph has been repeated with null payload mass and power, to check the sensitivity of the sizing solution to this parameter. The corresponding result is presented in Table 5.

The trends in the solution for different L_s reflect those found in Table 4, with generally mild relative reductions of the mass and geometric sizing compared to the case with payload. This result shows that the payload characteristics, at least for the considered range of values, typical to other applications for planetary exploration, are not significantly impacting the solution. This is expected, since the low density of the Martian atmosphere induces the need for a generally large lifting volume for sustaining the structural components of the airship (mostly the envelope) alone, which take a share of the overall mass significantly higher than the payload.

4.4.2. Effect of envelope material

Elaborating further on the comment just given to Table 5, the share of the overall mass pertaining to its components (grouped for convenience, with respect to Eq. (1)), is presented in Fig. 9 for the initial sizing for $L_s = 180°$ (Table 4).

Confirming the speculation introduced in the previous paragraph (Section 4.4.1), the envelope is taking over 80% of the overall mass. In order to try reducing this major driver in the mass (hence size) of the airship, the safety factor employed for the computation of the maximum stress, originally set to 4.0 as suggested by regulations (as mentioned in Section 4.2), is tentatively reduced to 2.0. This quantity, as explained, is employed as a multiplier of the estimated maximum stress that the envelope needs to sustain, and impacts the value of the areal density of the selected material. The sizing results corresponding to this modification are reported in Table 6.

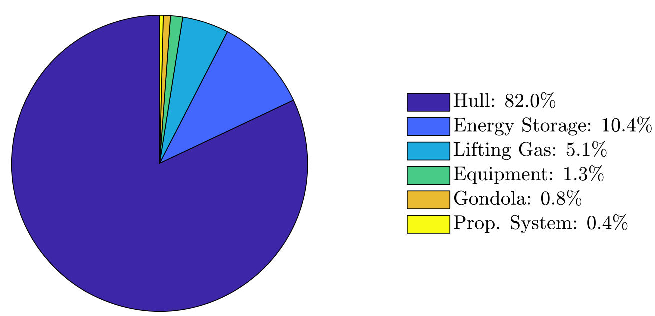

Fig. 9. Mass break-down of sizing solution from Table 4 at $L_s = 180°$.

Table 7
Mass breakdowns of the solutions from Table 6.

L_s [°]	m_{env} [kg]	m_{mot} [kg]	m_{mnt} [kg]	m_{prop} [kg]	m_{sc} [kg]	m_{strg} [kg]	m_{lg} [kg]
0	302	0.90	1.23	0.12	44.96	17.55	22.47
30	209	1.03	1.72	0.40	6.13	0.00	14.58
60	227	1.19	2.01	0.49	3.98	0.00	17.21
90	356	1.22	2.06	0.50	3.84	0.00	30.66
120	545	0.90	1.43	0.23	2.53	0.00	51.00
135	553	0.90	1.43	0.30	3.63	0.00	50.90
150	473	1.61	2.75	0.68	8.49	0.00	40.02
180	623	1.88	3.20	0.79	118.62	48.91	51.66

From Table 6, the solution has improved significantly for whatever solar longitude compared to Table 4, in terms of both geometrical sizing (in particular L) and mass. Notably, a general reduction of the fineness ratio is observed, together with a generally different geometry of the solar cells. The overall general arrangement of the components produces oscillating values of the mass for missions tailored to a specific solar

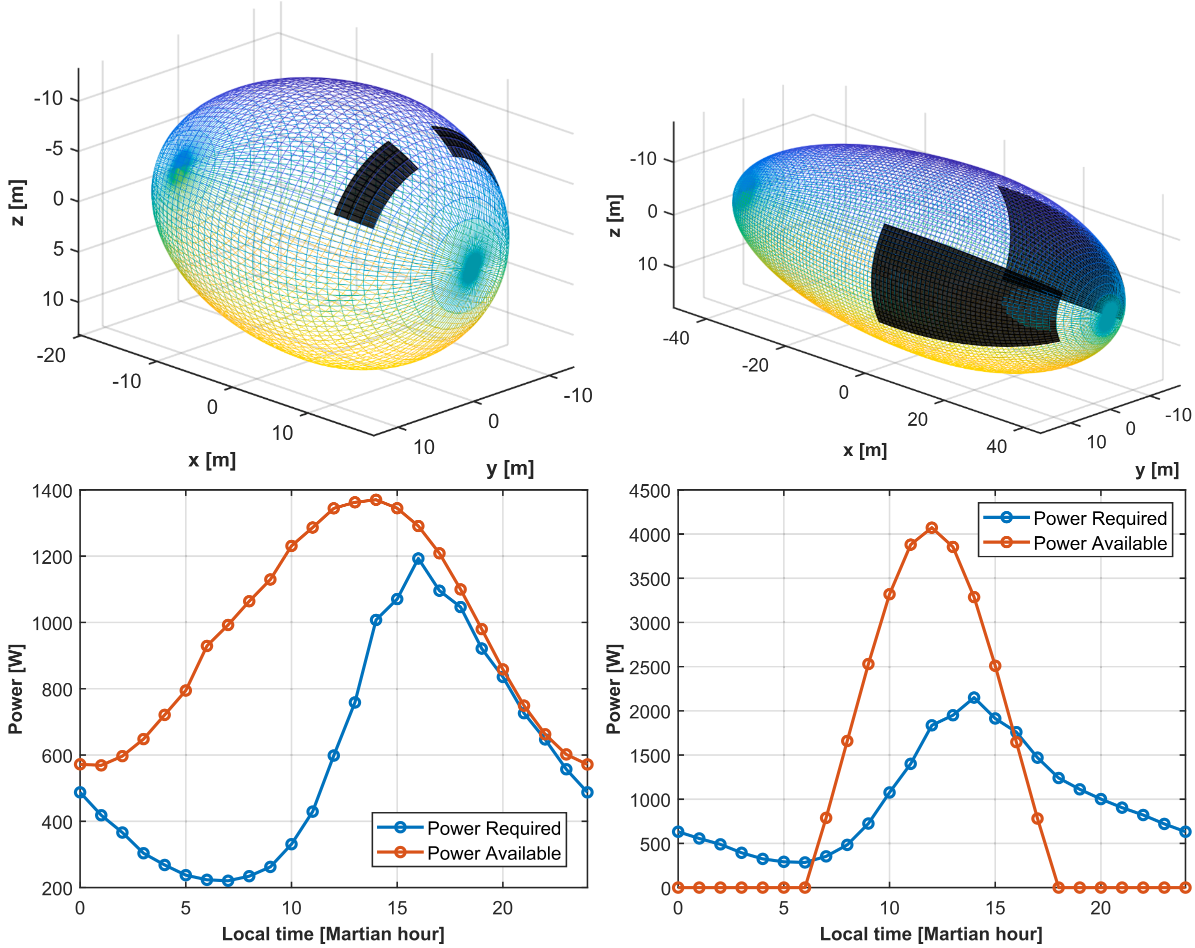

Fig. 10. Airship optimal design for $L_s = 30°$ (left) and $L_s = 180°$ (right). Top: geometrical sizing of the envelope and solar cells. Bottom plot: power available (from solar harvesting) and required over time.

longitude. The breakdown of the masses of the main components is reported in Table 7, where m_{env} is the mass of the envelope, m_{mot} is the mass of the electric motor(s), m_{mnt} is the mass of the engines mounts, m_{prop} is the mass of the propeller(s), m_{sc} is the mass of the solar cells, m_{strg} is the mass of the energy storage subsystem and m_{lg} is the mass of the lifting gas contained in the envelope.

Two examples of sizing solutions, pertaining to $L_s = 30°$ and 180°, are reported in Fig. 10, showing the shape of the envelope and the arrangement of the cells, as well as the time history of power required and power available from solar harvesting.

The evolution in the former is influenced mostly by the wind, which changes over time. When the power available from the solar source is below the power required, the batteries cover the requirement. In Fig. 10, this happens in the $L_s = 180°$ case (right plots), and not for $L_s = 30°$, yielding correspondingly starkly different solutions in terms of E_{bat} (Table 6).

4.4.3. *Coping with density change and effect of ballonets*

As mentioned in Section 3.1, the seasonal change of the density on Mars is non-negligible, and for the coordinates chosen for this research, its evolution is shown on the left plot in Fig. 11 as a function of the solar longitude. A change in the atmospheric density would produce a change in the buoyancy experienced by the airship, itself leading to a change in the floating altitude. Compared to the terrestrial atmosphere however, the case of Mars is more critical. The right plot on Fig. 11 displays the behavior of the density with the altitude for several values of L_s. As a reference, the density at $L_s = 0°$ is plotted as a dashed line. From this plot, the density on the surface (i.e., the top achievable at a given L_s) is for $L_s = 120°$, 150° below the value of density for 2,000 m at $L_s = 0°$. This means that an airship designed for a stationing phase at 2,000 m at $L_s = 0°$, when $L_s = 120°$, 150°, would not find the density needed for floating before reaching anywhere above the surface.

This clearly indicates that, for an airship capable of flying missions extending over a span of months, or in general without restrictions in coping with the environmental conditions pertaining to a different L_s, a buoyancy management system is imperative. The only largely tested such system in conjunction with a super-pressure balloon is a ballonet system [61]. For a station-keeping mission at altitude, the internal bags, communicating with the atmospheric environment via a set of valves, are filled with atmospheric mixture to increase the density, or emptied to decrease it, in order to keep the density of the gases within the envelope (lifting gas plus atmospheric gas in the ballonets) to the level of the atmospheric density at the desired altitude. Therefore, when the density of the atmosphere changes, the internal density of the airship envelope is changed, and static equilibrium is preserved correspondingly. At the level of preliminary sizing, it is possible to model the presence of this system through the corresponding mass, due mostly to the envelope of the additional inner bags, valves and ducts. Not much modern data exist to the knowledge of the authors, and statistical regressions are employed instead [61], leading to a material mass of the ballonet of 11 kg/m^2 (which accounts for the film material of the ballonet itself and for the associated systems). The maximum change in the ballonet inflation volume takes a time corresponding to the change in the solar longitude between the maximum and minimum atmospheric density, which from

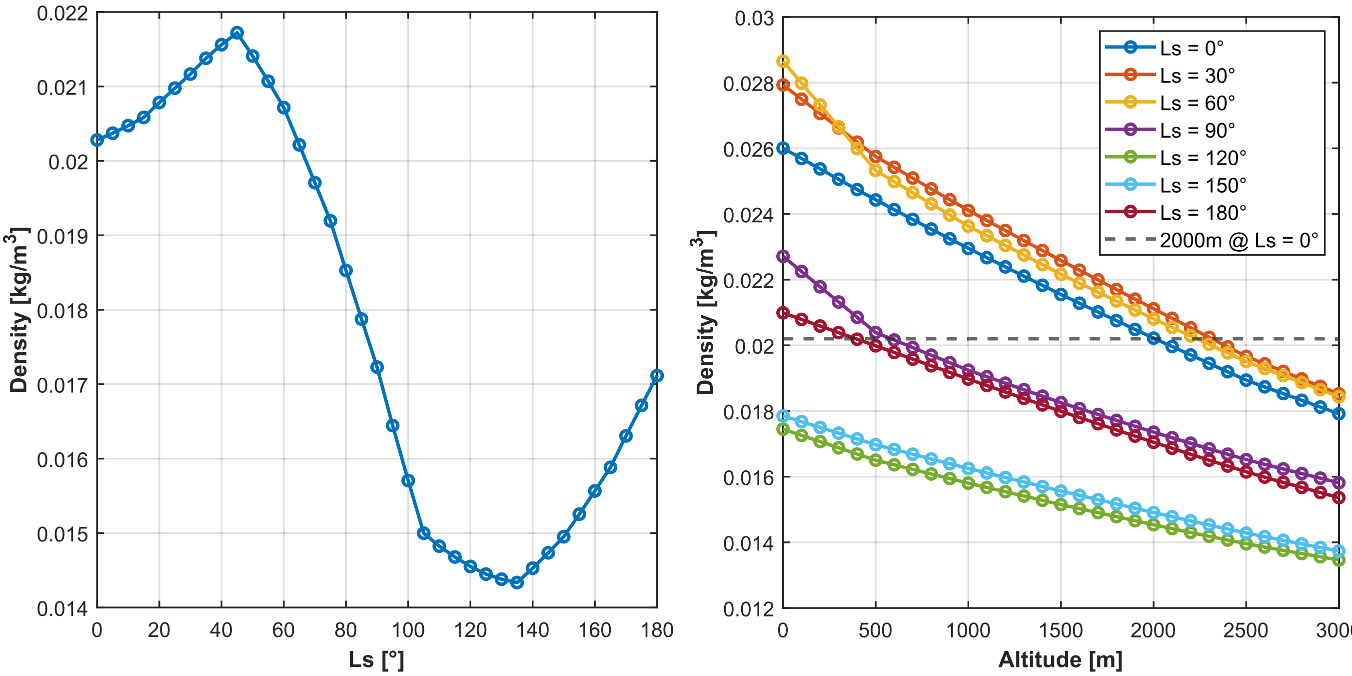

Fig. 11. Atmospheric density for the considered mission coordinates. Left: at 2,000 m altitude as a function of the solar longitude L_s. Right: as a function of the altitude, for different values of L_s (colored lines). Dashed line: density at L_s = 0°, 2,000 m.

Table 8
Sizing solution with ballonets.

L_s [°]	L [m]	f [-]	x_{le} [m]	x_{te} [m]	θ_{in} [rad]	θ_{out} [rad]	m [kg]	E_{bat} [kWh]	σ_{lim} [N/cm]
135	151.3	1.95	5.0	7.16	0.50	1.918	6790	0	221.63

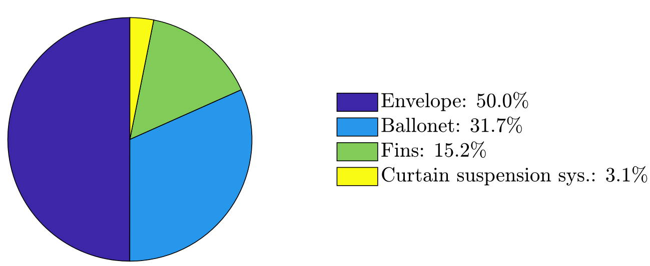

Fig. 12. Mass break-down of hull components in presence of ballonets (sizing results in Table 8).

Fig. 11 (left) amounts to 200 Earth days, yielding a non-critical, very low air flow.

For a tentative sizing of the airship with ballonets, the condition at L_s = 135° is considered, yielding from Fig. 11 the absolute minimum density found at 2,000 m (design stationing altitude). The corresponding sizing is presented in Table 8, to be compared with the corresponding line on Table 6, taken as a reference.

Notably, the increase in mass with respect to the solution without ballonets (Table 6) is almost ten-fold. In this scenario, the mass of the hull (i.e., the envelope, ballonets, fins and internal structure) accounts for 92.6% of the overall mass of the airship. As shown in Fig. 12, this increase is triggered by the additional, non-buoyant mass of the ballonets, which in the sizing solution accounts for almost one-third of the overall hull, which in turns corresponds to a bigger mass (ensuing from a bigger geometrical sizing) for exerting a sufficient buoyant force for flight.

The increase in the overall length of the system appears similarly critical as that of the mass. It should be noted from the sizing solution in Table 8 that the mass of the energy system is null. The result shown on the table accounts for the worst day only, when despite the lowest density is recorded, the available vs. required power profile is favorable. An extension of the sizing solution to cope with the power profile found over the complete span of solar longitude values L_s composing a multi-month mission would be even less feasible than the already critical solution proposed here, due to the additional battery mass.

4.4.4. *Effect of propeller performance*

All the above computations have been carried out with a propeller efficiency of η_P = 80%, a standard achievable value for terrestrial applications [65]. However, the different conditions faced by a rotor in the Martian atmosphere, mostly due to the very reduced Reynolds number, produce geometrical solutions and performance levels significantly far from Earth values.

For the present analysis, the Reynolds number can been estimated based on the density and kinematic viscosity of the atmosphere for the assumed coordinates and altitude.

Preliminarily, the effect of propeller diameter on the efficiency η_P has been tested out of the airship sizing algorithm. Employing blade-element momentum theory, considering a blade with an assigned single airfoil taken as a Selig S2060, a typical low-Reynolds airfoil [66], the behavior of a propeller with optimal efficiency was first investigated. Different diameters have been tested, for Reynolds between Re = 25,000 and Re = 75,000, corresponding to the values of interest for this application, and the behavior has been checked as a function of the spinning rate (Ω). Initially, a single propeller has been assumed, for the known value of the thrust needed for an already sized airship to counter the wind, in a station-keeping mission. The results are shown in Fig. 13, and they highlight that the effect of the RPM is not so significant compared to that of the diameter, in determining the value of η_P. However, the diameter of all sizing solutions appears too high for

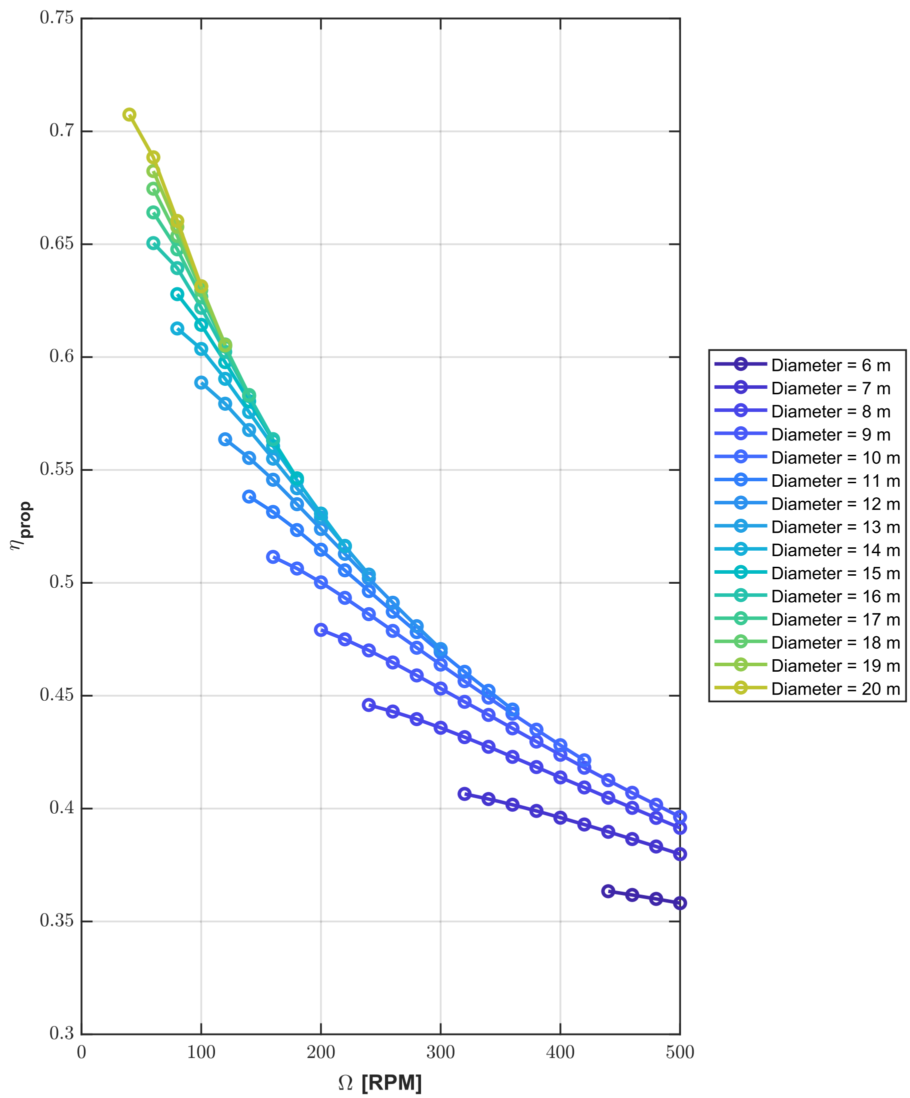

Fig. 13. Propeller efficiency η_P for 2-bladed propellers with different diameter, as a function of the rotational speed Ω. Range corresponding to a condition of $25,000 < Re < 75,000$.

any practical application. Correspondingly, in order to avoid unrealistically high values of the diameter, which would be hard to hypothesize for an application on Mars, due to transportation issues from the Earth of geometrically big components, it was chosen to operate with four smaller propellers, instead of a single larger one. This reduces proportionately the value of the thrust to be exerted by a single rotor, and correspondingly the diameter. For the same reason (i.e., less components), a two-blade propeller was considered, after numerically checking that the advantage of having more blades (2 to 10 was tested) is negligible on η_P.

Then, two airship design conditions have been considered, at $L_s = 0°$, 135°, and a preliminary sizing of a propeller has been carried out correspondingly. The environmental conditions are displayed in Table 9. The value of η_P has been changed tentatively by hand within the airship sizing algorithm, yielding a value of thrust employed for the sizing of the propeller. The latter has been employed for designing the propeller geometry, which in turns returns a value of η_P. This triggers a new computation of the airship sizing. The values of thrust shown in Table 9 correspond to a converged solution.

The corresponding top value of the propeller efficiency, considering four propellers and the corresponding down-scale of the thrust per propeller with respect to employing a single propeller, is respectively $\eta_P = 0.375$ for the $L_s = 0°$ case, and $\eta_P = 0.268$ for the $L_s = 135°$ case. The actual results of the propeller sizing in the two cases are reported in Appendix A.

Table 9
Considered atmospheric conditions and thrust (overall) for propeller design.

L_s [°]	ρ_{atm} [kg/m^3]	ν_{atm} [m^2/s]	a [m/s]	V_{wind} [m/s]	T_{prop} [N]
0	0.0202	$3.63\cdot10^{-4}$	190.40	5.67	32.54
135	0.0143	$7.47\cdot10^{-4}$	227.61	6.43	71.22

The outcome of the airship sizing pertaining to these two settings of the propeller efficiency are reported in Table 10. These should be compared to the results in Table 6, since ballonets are left out of the design for this computation.

It can be noted that the overall sizing of the airship is minimally affected by the propeller efficiency. This is expected, since differently from fixed-wing or rotary-wing machines, the airship does not rely on propulsion for flight.

Table 10
Airship sizing results (with no ballonets) and purpose-designed propellers.

L_s [°]	L [m]	f [-]	x_{le} [m]	x_{te} [m]	θ_{in} [rad]	θ_{out} [rad]	m [kg]	E_{bat} [kWh]	σ_{lim} [N/cm]
0	57.7	1.96	5.0	13.4	0.50	6.28	529	4.70	82.93
135	61.6	1.49	5.0	8.41	0.50	2.07	789	0.00	117.6

5. Conclusions

The present research has investigated some relevant aspects concerning the feasibility of an airship as a platform for the exploration of Mars. Starting with a selection of that planet for its more favorable atmospheric conditions for the exploitation of the inherent features of an airship (both buoyancy and controllability, as opposed to balloons, which are not controllable) compared in particular to Venus, a preliminary sizing methodology for an airship on Mars has been set up. The background for it was found in the method employed for terrestrial high-altitude airship applications, which however required significant amendments for coping with the proposed new application. Besides changed data for the atmosphere with respect to Earth, methodological amendments are constituted by a more complete modeling of the solar irradiance, as well as by a more accurate modeling of the solar panels, accounting for their layers, and the adoption of a dynamic thermal model for the solar array, envelope and lifting gas. Additionally, ballonets have been included with a simple model in the airship sizing, and the actual performance of propellers for the Martian environment has been predicted and taken into account for airship sizing analyses.

A mission corresponding to a one-day (midnight-to-midnight) exploration has been considered for studying the effects of the environmental conditions (including irradiance) on the outcome of the airship sizing procedure. A geologically relevant, yet morphologically complex location has been considered, yielding an interesting practical case for this preliminary analysis. The position over the northern polar cap of Mars is favorable from the standpoint of irradiance, being interested by midnight Sun for most solar longitude of the season of interest (i.e., out of dust storm time frames featured in the Martian winter in the area).

The outcome of the sizing can be summarized as follows. For the considered payload, assuming momentarily not to include a ballonet system, the airship sizing is fairly dependent on the solar longitude, topping at the level of some tonnes of mass and an overall length of more than 160 m, hardly feasible in a real application, mostly due to the material and thickness of the envelope, sized to guarantee a safety margin taken from civil aviation regulations. When halved, this safety factor produces a sizing topping at 1 ton and less than 100 m for the least favorable solar longitude, and reaching down to roughly 300 kg and 40 m for the most favorable. The payload, considering the range of some tens kilograms typical to monitoring missions, has only a very minor effect on the sizing, similar to the batteries. An analysis of the behavior of the atmospheric density on Mars, and in particular its evolution over time with seasonal cycles, shows that a buoyancy regulation system would be strictly required to cope with the extreme changes in density encountered on the planet. Considering ballonets for the task and including them in the airship sizing procedure, the sizing solution tends to be once again dramatically increased in terms of mass and corresponding geometrical dimensions. Care has been taken to analyze the effect of the geometrical sizing of a propeller such to cope with the Martian atmospheric conditions (notably, implying a range of Reynolds values not typical to propellers employed on Earth), and such to be potentially transportable to the planet. However, despite a significantly reduced efficiency is found compared to the values attained on Earth, no relevant effects have been found on the airships sizing, as expected, since propulsion is not strictly related to countering weight on an airship.

In view of the results obtained in this study, it appears that even in the least favorable combination of position on/over the surface and of solar longitude, the mass of an airship platform, when considering a one-day mission for which the design is optimized, is comparable to that of a land rover (reaching 1,020 kg in the worst case, compared to 1,025 kg of the Perseverance land rover). However, the rather large geometrical sizing and volume to be filled would impose a prominent effort especially in the inflation and terminal maneuvering phases in proximity with the ground. An airship capable of coping with longer missions and generic values of the solar longitude would be associated to an even more requiring sizing solution. Considered in the context of the available literature concerning Martian airships, this work provides a clear insight on how a detailed study, even considering favorable conditions (i.e. midnight Sun), leads to doubts regarding the feasibility of a global mission (i.e. lasting over multiple solar longitudes). Key technological parameters substantially influencing the solution appear to be the material employed for the envelope, as well as the overall technology adopted for buoyancy management. Traditional ballonets, in particular, appear to be exceedingly heavy, indicating a possible line of further research, currently of great interest also for terrestrial applications (i.e. buoyancy control techniques).

CRediT authorship contribution statement

Carlo E.D. Riboldi: Writing – review & editing, Writing – original draft, Supervision, Resources, Methodology, Investigation, Formal analysis, Conceptualization; **Daniele Marcora:** Writing – review & editing, Visualization, Validation, Software, Methodology, Investigation, Formal analysis, Data curation, Conceptualization.

Data availability

Data will be made available on request.

Declaration of competing interests

The authors declare that they have no known competing financial interests or personal relationships that could have appeared to influence the work reported in this paper.

Funding

This research did not receive any specific grant from funding agencies in the public, commercial, or not-for-profit sectors.

Appendix A. Results of propeller design

The propeller sizing solutions corresponding to the two design examples presented in Section 4.4.4 are reported here. The design point in terms of atmospheric conditions, including wind speed (which amounts to the airspeed in a station-keeping mission) are those reported in Table 9. As explained, the propeller diameter has been set to 2 m, and the propeller is two-bladed. The blade features a single Selig 2060 airfoil, and the root incidence has been set to 3°. For the sake of clarity, computations have been carried out accounting for the actual Reynolds number at every spanwise station along the blade, i.e. accounting for the local value of the speed induced by rotation.

The main coefficients involved in the analysis are gathered in Table A.1, along with their definitions.

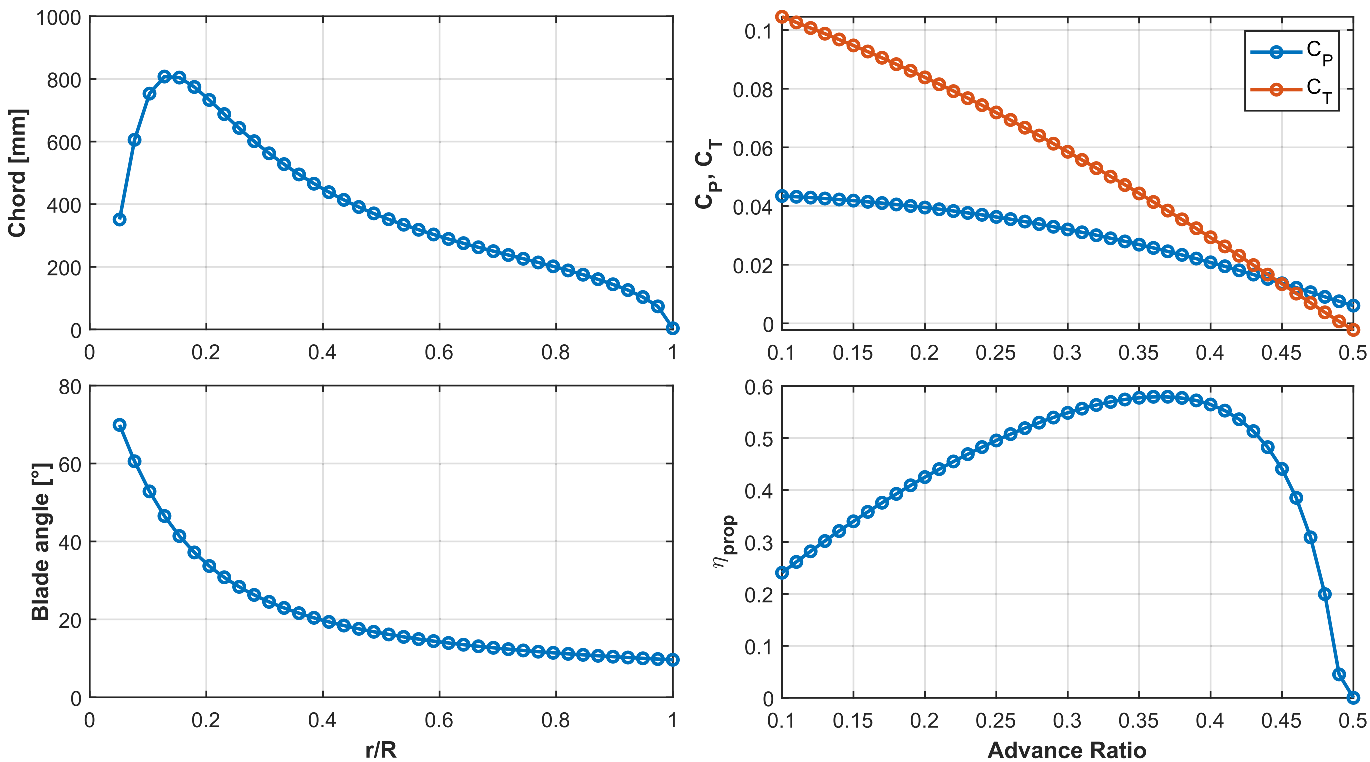

Fig. A.1. C_P, C_T, η_P, chord and twist distribution at $L_s = 0°$.

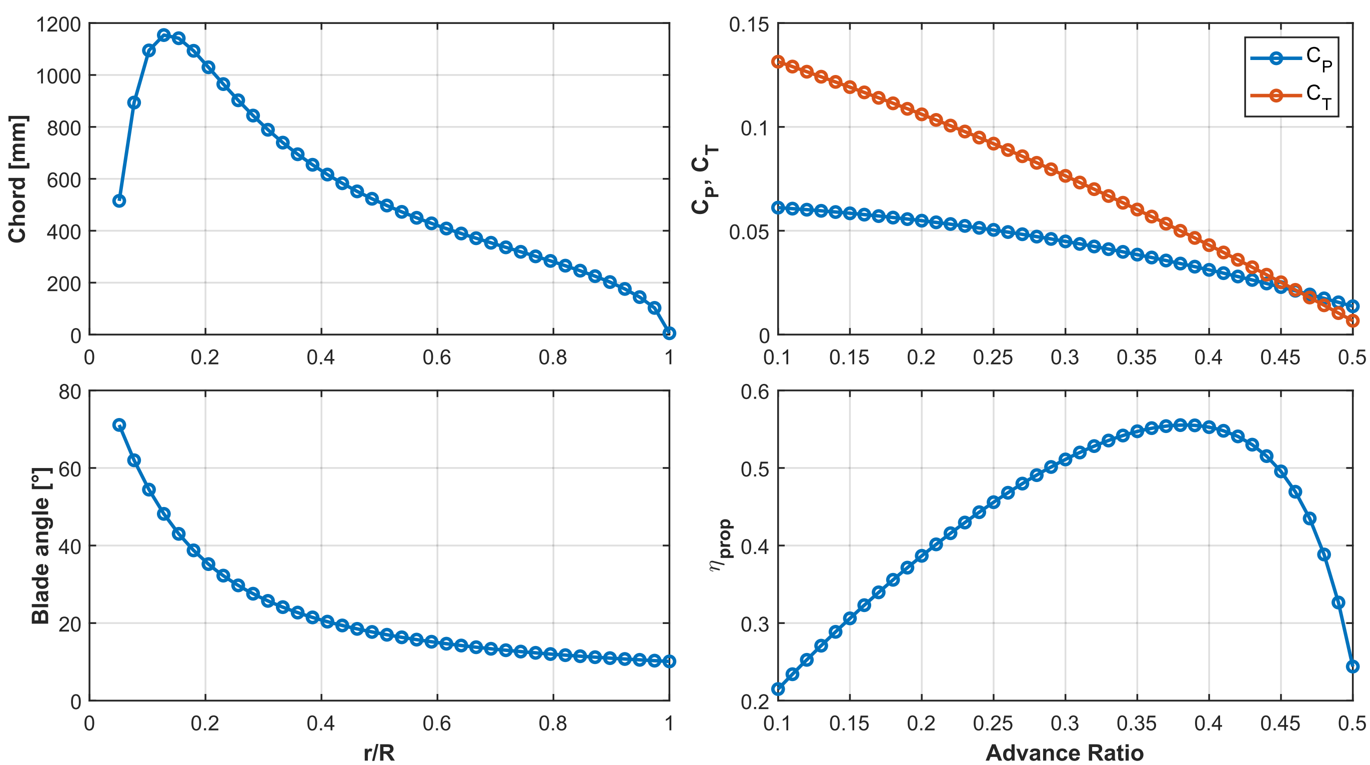

Fig. A.2. C_P, C_T, η_P, chord and twist distribution at $L_s = 135°$.

In Table A.1, V_∞ represents the axial inflow speed, D the propeller diameter, ρ the density of the atmosphere, T the thrust, P the power and RPM the revolutions per minute.

For the case at $L_s = 0°$, Fig. A.1 displays the chord and twist distributions (top and bottom left) as functions of the relative spanwise position r/R, as well as power and thrust coefficients (C_P and C_T respectively) and efficiency η_P as functions of the advance ratio (top and bottom right). Fig. A.2 displays the same results for the case at $L_s = 135°$.

Fig. A.3 shows for both cases the dependence of the efficiency from the rotational rate Ω, obtained from the advance ratio on account of the assigned diameter and wind speed (equal to the undisturbed airspeed

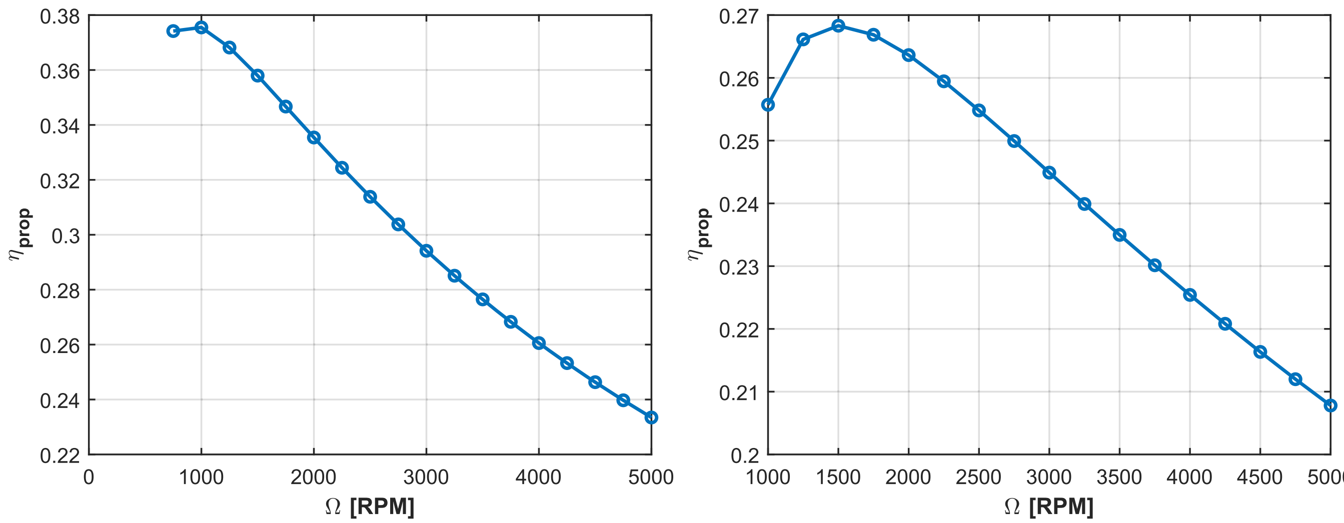

Fig. A.3. Propeller efficiency η_P as a function of Ω, for $L_s = 0°$ (left) and $L_s = 135°$ (right).

Table A.1
Definitions of performance coefficients for propeller design.

Description	Definition
Revolutions per second	$n = \frac{RPM}{60}$
Advance Ratio	$J = \frac{V_\infty}{n\ D}$
Thrust Coefficient	$C_T = \frac{T}{\rho\ n^2\ D^4}$
Power Coefficient	$C_P = \frac{P}{\rho\ n^3\ D^5}$
Propeller efficiency	$\eta_{prop} = \frac{C_T}{C_P}\ J$

in this station-keeping case). Each point on these plots corresponds to a different propeller, optimized for the rotational rate on the horizontal axis. The two top-efficiency values imported in Section 4.4.4 can be retrieved for $\Omega = 1{,}000$ rpm and $\Omega = 1{,}500$ rpm respectively for the two considered solar longitudes.

It can be noted that the chord geometry includes a very relevant chord for span-wise positions relatively close to the root (up to roughly $r/R = 30\%$). To reduce the constructive complexity, the computation of the performance of the propeller has been re-run trimming the inner portion of the propeller below a diameter of 0.5 m from the spinning axis, loosing less than 1% point on η_P and yielding a significant reduction of the maximum chord (this way, lowered to 0.6 m for $L_s = 0°$ and 0.8 m for the $L_s = 135°$ case).

Appendix B. Miscellaneous parameters and settings

In Table B.1 is reported a schematic view of the most relevant baseline parameters and settings employed within the methodology, not previously mentioned in the body of the work.

The 6.1 version of the Mars Climate Database has been employed, with an average climatology solar and dust scenario.

Table B.1
Values and settings.

Battery Parameter	Symbol	Value
Charge efficiency	η_{ch}	0.96
Discharge efficiency	η_{dsch}	0.96
Depth of discharge	DoD	0.95
Specific energy [J/kg]	W_{strg}	$250 \times 3.6 \times 10^3$
Energy density [J/m^3]	ρ_{strg}	$570 \times 3.6 \times 10^6$
Energy safety factor	K_{energy}	1.1
Transmission efficiency	η_{trans}	0.98
Power switch/step efficiency	η_{swch}	0.90
Solar Cells Parameter	Symbol	Value
Packing efficiency	η_{pack}	0.90
Mass/area ratio [kg/m^2]	ρ_{sc}	0.07
Mass multiplicative factor	K_{sc}	1.3
Lifting Gas Parameter	Symbol	Value
Purity [%]	LGP	100
Pressure difference safety factor	P_{SF}	1.5
Envelope and Fins Parameter	Symbol	Value
Envelope mass multiplicative factor	K_{env}	1.2
Fin area to airship volume ratio	R_{fa}	0.0121
Fin mass multiplicative factor	K_{fin}	2
Propulsion System Parameter	Symbol	Value
Engines mount mass-to-engines mass ratio	W_{mnt}	1.2

Appendix C. Additional sensitivity studies

Some considerations on the sensitivity of the thermal model have been made. Given that most of the thermal parameters are directly taken from the physics of the materials, the black globe temperature of the environment T_{bb} was chosen for the assessment. This is due to the fact that the estimation of it as 60% of the atmospheric temperature comes from a simplified regression of in-situ measurements, of possibly limited accuracy to the present case. For comparison, results were produced by evaluating the optimal designs at $L_s = 30°$ and 180° from Table 6 in the case of $T_{bb} = T_{atm}$.The outcome of the test is presented in Table C.1

Table C.1
Sensitivity to the parameters of the thermal model.

L_s	Length [m] (T_{bb} = 0.6 T_{atm})	Length [m] ($T_{bb} = T_{atm}$)	Mass [kg] (T_{bb} = 0.6 T_{atm})	Mass [kg] ($T_{bb} = T_{atm}$)
30°	39.1	39.4	301	306
180°	92.6	92.8	1020	1025

Even though the change has an unavoidable impact on the fluxes (the radiation ones in particular), which in turns reflects on different temperatures and solar cells efficiency, it is clear how this has only a mild effect on the final design results.

Similarly, some considerations on the sensitivity of the sizing solution to drifts in the environmental model were carried out. For example, 50% stronger winds were applied to the optimal designs at $L_s = 30°$ and 180° from Table 6 and new design points were found, as reported in Table C.2.

Table C.2
Sensitivity to wind intensity.

L_s	Length [m] (MCD data)	Length [m] (MCD data + 50%)	Mass [kg] (MCD data)	Mass [kg] (MCD data + 50%)
30°	39.1	47.4	301	349
180°	92.6	145.6	1020	2304

As one would expect, size grows by a fairly amount as the wind speed (and therefore the thrust required for station keeping) grows. This is particularly true for the $L_s = 180°$ case, where a non negligible energy storage is required. This conclusion is rather synthetic, but it serves to show how the model as a whole follows a logical and quite predictable behavior, which supports the credibility of the conclusions regarding the globally limited feasibility of the concept, in turns induced by the need for an exceedingly heavy buoyancy control system.

References

[1] C.E.D. Riboldi, A. Rolando, Layout analysis and optimization of airships with thrust-based stability augmentation, Aerospace 9 (2022) 393. https://doi.org/10.3390/aerospace9070393
[2] C.E.D. Riboldi, A. Rolando, Thrust-based stabilization and guidance for airships without thrust-vectoring, Aerospace 10 (2023). https://doi.org/10.3390/aerospace10040344
[3] C.E.D. Riboldi, A. Rolando, Autonomous flight in near hover and hover for thrust controlled unmanned airships, Drones 7 (2023). https://doi.org/10.3390/drones7090545
[4] Kelluu Oy, Metallimiehentie, 4, Reijola, Finland, 80330. kelluu.com, accessed Jan. 2026.
[5] HyLight, Brétigny-sur-Orge, France, 91220. www.hylight.aero, accessed Jan. 2026.
[6] FloFleet, Via Sebenico, 24, Milan, Italy, 20124. www.flofleet.com, accessed Jan. 2026.
[7] C.E.D. Riboldi, M. Belan, S. Cacciola, R. Terenzi, S. Trovato, D. Usuelli, G. Familiari, Preliminary sizing of a low-altitude airship including ion-plasma thrusters, in: 34th Congress of the International Council of the Aeronautical Sciences (ICAS2024), 9–13 September 2024, Florence, Italy, 2024, pp. 1–20.
[8] P. Gili, M. Civera, R. Roy, C. Surace, An unmanned lighter-than-air platform for large scale land monitoring, Remote Sens. 13 (13) (2021) 2523.
[9] P. Gili, L. Castronovo, M. Civera, R. Roy, C. Surace, A multidisciplinary design optimisation (MDO) algorithm for the automatic sizing of an unmanned lighter-than-air platform, in: Lighter than Air Systems, Springer Nature Singapore, 2023, pp. 147–155.
[10] C.E.D. Riboldi, L. Fanchini, Assessing the technical–economic feasibility of low-altitude unmanned airships: methodology and comparative case studies, Aerospace 12 (2025) 244. https://doi.org/10.3390/aerospace12030244
[11] Various, Stratobus autonomous stratospheric airship, 2020, https://www.airforce-technology.com/projects/stratobus/.
[12] P. Lobner, HiSentinel Stratospheric Airships, Tech. rep., Lyncean Group of San Diego, 2020.
[13] C.E.D. Riboldi, A. Rolando, G. Regazzoni, On the feasibility of a launcher-deployable high-altitude airship: effects of design constraints in an optimal sizing framework, Aerospace 9 (2022) 1–37. https://doi.org/10.3390/aerospace9040210
[14] C.E.D. Riboldi, A. Rolando, S. Cacciola, G. Regazzoni, I. Spadafora, On the optimal preliminary design of high-altitude airships: automated procedure and the effect of constraints, in: Aerospace Europe Conference 2023 - 10th EUCASS - 9th CEAS, 9–13 July 2023, Lausanne, Switzerland, 2023, pp. 1–15.
[15] C.E.D. Riboldi, M. Belan, S. Cacciola, R. Terenzi, S. Trovato, D. Usuelli, G. Familiari, Preliminary sizing of high-altitude airships featuring atmospheric ionic thrusters: an initial feasibility assessment, Aerospace (2024). https://doi.org/10.3390/aerospace11070590
[16] V.V. Kerzhanovich, J.A. Cutts, Aerobots in planetary exploration, in: Proceedings of the 2000 IEEE Aerospace Conference, 25 March 2000, Big Sky, MT, 2000, p. 547–555. https://doi.org/10.1109/AERO.2000.879322
[17] Various, Vision and Voyages for Planetary Science for the Decade 2013–2022, Tech. Rep. 978-0-309-22464-2, Space Studies Board, National Research Council, The Keck Center of the National Academies, Washington, DC, 2011.
[18] A. Colozza, Airships for Planetary Explorations, Technical Report NASA/CR—2004-213345, Analex Corp., Brook Park, OH, 2004.
[19] C.T. Stelzried, R.A. Preston, C.E. Hildebrand, J.H. Wilcher, J. Ellis, The Venus Balloon Project, Technical Report TDAProgressReport 42-8, The Telecommunications and Data Acquisition Report, 1986.
[20] A. Arredondo, A. Hodges, J.N.H. Abrahams, C.C. Bedford, B.D. Boatwright, J. Buz, C. Cantrall, J. Clark, A. Erwin, S. Krishnamoorthy, VALENTInE: a concept for a new frontiers-class long-duration in situ balloonbased aerobot mission to Venus, Planet. Sci. J. (2022). https://doi.org/10.3847/PSJ/ac7324
[21] S. Lewis, J. Holmes, Martian Meteorology, Technical Report, Royal Meteorological Society, 2021.
[22] NASA, Mars Facts - science.nasa.gov/mars/facts/, accessed Jan. 2026.
[23] D. Banfield, S.S. Johnson, J. Stern, D. Brain, P. Withers, R. Wordsworth, S. Ruff, R.A. Yingst, J. Bleacher, R. Whitley, D.W. Beaty, S. Diniega, R. Zurek, Mars Scientific Goals, Objectives, Investigations, and Priorities, Technical Report, Mars Exploration Program Analysis Group (MEPAG), 2018.
[24] W.J.F. Koning, M. Dominguez, Mars Helicopter Ingenuity Rotor Geometry, Technical Report, NASA Ames Research Center, Moffett Field, CA, 2024.
[25] W. Johnson, S. Withrow-Maser, L. Young, C. Malpica, W.J.F. Koning, W. Kuang, M. Fehler, A. Tuano, A. Chan, A. Datta, C. Chi, R. Lumba, D. Escobar, J. Balaram, T. Tzanetos, A.F. Grip, Mars Science Helicopter Conceptual Design, Technical Report, NASA Ames Research Center, Moffett Field, CA, 2020.
[26] A.R. Girerd, A case for a robotic Martian airship, in: 12th Lighter-Than-Air Systems Technology Conference, 3–5 June 1997, San Francisco, CA, 1997, pp. 1460.
[27] K. Shrotri, K. Manyapu, A. Khalid, Y.F. Sumer, M.E. Gunduz, D.P. Schrage, MARVIN - near surface methane detection on Mars, in: 2007 IEEE Aerospace Conference, 3–10 March 2007, Big Sky, MT, 2007, pp. 1–16.
[28] J.P. Clarke, J. Rimoli, J.T. Gloyd, H. Logarzo, J. Kraus, Evacuated Airship for Mars Missions: NIAC Phase I, 2017, Technical Report HQ-E-DAA-TN58817, Georgia Tech Air Transportation Library, 2018.
[29] Y. Pozhanka, M. Hassanalian, The potential of airships as a scientifically valuable tool for Mars exploration missions and information transfer, in: AIAA Scitech 2025 Forum, 6–10 January 2025, Orlando, FL, 2025, p. 2733.
[30] E. Millour, F. Forget, A. Spiga, T. Pierron, A. Bierjon, L. Montabone, M. Vals, F. Lefèvre, J.Y. Chaufray, M. Lopez-Valverde, F. Gonzalez-Galindo, S. Lewis, P. Read, M.C. Desjean, F. Cipriani, The Mars climate database (version 6.1), in: Europlanet Science Congress 2022, September 2022, Granada, Spain, 2022.
[31] F. Forget, E. Millour, T. Pierron, A. Bierjon, Mars Climate Database v6.1 Validation Document, Technical Report ESA Contract No.4000128572/19/NL/AS, CNES/ESA, 2022.
[32] R. Bardera, Mars Exploration - a Step Forward, IntechOpen, 2020. https://doi.org/10.5772/intechopen.90912
[33] Various, Gas constant - NASA, Planetary Data System (PDS): the planetary atmospheres node, 2025. https://pds-atmospheres.nmsu.edu/
[34] J. Appelbaum, D.J. Flood, Solar Radiation on Mars, Technical Report E-5783, NASA Lewis Research Center, Cleveland, OH, 1990.
[35] J. Meeus, Astronomical Algorithms, Willman-Bell, Inc., Richmond, VA, 1990.
[36] J. Martin, G. Soffen, Viking 1 Early Results, Tech. Rep. SP-408, NASA Scientific and Technical Information Office, Washington, D.C., 1977.
[37] G.W. Petty, First Course in Atmospheric Radiation, Sundog Publishing, LLC, Madison, WI, 2004.
[38] J.B. Pollack, R.M. Haberle, J. Schaeffer, H. Lee, Simulations of the general circulation of the Martian atmosphere: 1. Polar processes, J. Geophys. Res. Solid Earth 95 (1990) 1447–1473.
[39] E.A. Silk, Introduction to Spacecraft Thermal Design, Cambridge University Press, Cambridge, UK, 2020.
[40] T.D. Lee, A.U. Ebong, A review of thin film solar cell technologies and challenges, Renew. Sustain. Energy Rev. 70 (2017). https://doi.org/10.1016/j.rser.2016.12.028
[41] Ascent Solar Technologies, Inc., Thornton, CO. www.ascentsolar.com, accessed Jan. 2026.
[42] J.G. Smith, J.W. Connell, K.A. Watson, P.M. Danehy, Optical and Thermo-optical Properties of Polyimide-Single-Walled Carbon Nanotube Films: Experimental Results and Empirical Equations, Technical Report LF99-687, NASA Langley Research Center, Hampton, VA, 2005.
[43] Various, DuPont Kapton HN polyimide, Technical Report K-15345 03/06, DuPont, 2006.
[44] M. Barragán Sánchez-Lanuza, I. Lillo-Bravo, S. Moreno-Tejera, J.L. Sancho Rodríguez, J.-M. Delgado-Sanchez, Experimental CIGS technology performance under low concentration photovoltaic conditions, J. Clean. Prod. 446 (2024) 141384.
[45] S. Nofal, T.S. Vaas, U. Rau, B.E. Pieters, An electro-thermal finite element method (FEM) model for local hotspot kinetics in Cu(In, Ga)Se2 thin-film solar modules, J. Appl. Phys. 136 (2024) 115102.

[46] Various, Tefzel ETFE, Tech. Rep. C-11590, The Chemours Company, 2018.

[47] J.H. Henninger, Solar Absorptance and Thermal Emittance of Some Common Spacecraft Thermal Control Coatings, Technical Report N84-23698, NASA Scientific and Technical Information Branch, Washington, D.C., 1984.

[48] E. Matz, J. Appelbaum, Y. Taitel, D.J. Flood, Solar cell temperature on Mars, J. Propuls. Power 14 (1998).

[49] M.I. Alam, R.S. Pant, A multi-node model for transient heat transfer analysis of stratospheric airships, Adv. Space Res. 59 (2017) 3023–3035.

[50] M.I. Alam, A.A. Pasha, A.G.A. Jameel, U. Ahmed, High altitude airship: a review of thermal analyses and design approaches, Arch. Comput. Methods Eng. 30 (2023) 2289–2339.

[51] W. Zheng, X. Zhang, R. Ma, Y. Li, A simplified thermal model and comparison analysis for a stratospheric lighter-than-air vehicle, J. Heat Transf. 140 (2) (2018) 0228011–9.

[52] W. Zheng, Q. Zhou, Z. Lib, X. Zhang, Y. Liu, M. Li, Performance analysis of a novel stratospheric airship concept based on gas–liquid phase change, Appl. Therm. Eng. 159 (2019) 1137–48.

[53] S. Hong, G. Shanshan, Q. Xiaohui, Thermodynamics analysis of a stratospheric airship with hovering capability, Appl. Therm. Eng. 146 (2019) 600–607.

[54] L.A. Carlson, W.J. Horn, A new thermal and trajectory model for high altitude balloons, J. Aircr. 20 (1983) 500–507.

[55] K. Kadoya, N. Matsunaga, A. Nagashima, Viscosity and thermal conductivity of dry air in the gaseous phase, J. Phys. Chem. Ref. Data 14 (1985) 947–970.

[56] R.E. Farley, Balloon ascent: 3-D simulation tool for the ascent and float of high-altitude balloons, in: AIAA 16th Lighter-Than-Air and Balloon Systems Conference, 26–28 September 2005, Arlington, VA, 2005, pp. 1–15.

[57] R.M. Rapert, A Heat Transfer Model for a Hot Helium Airship, Technical Report AD-A183 786, Naval Post-Graduate School, Monterey, CA, 1987.

[58] C. Dull, L. Wagner, W. Johnson, L. Young, Hover and forward flight performance modeling of the ingenuity Mars helicopter, in: VFS Aeromechanics for Advanced Vertical Flight Technical Meeting, San Jose, CA, Jan 25–27, 2022.

[59] D.V. Kaweesa, G. Sahragard-Monfared, J. Bowman, Structural analysis of a Mars science helicopter blade: lessons learned, in: Vertical Flight Society's Vertical Lift Aircraft Design and Aeromechanics Specialists' Conference, San Jose, CA, USA, Jan. 27–29, 2026.

[60] N. Costa, M. Massironi, L. Penasa, S. Ferrari, R. Pozzobon, J. Nava, Geological maps of the nord rupes (north polar cap, Mars), Geol. Field Trips Maps 16 (2024) 1–17.

[61] G.E. Carichner, L.M. Nicolai, Fundamentals of Aircraft and Airship Design, AIAA Education Series, American Institute of Aeronautics and Astronautics, Inc., 2013.

[62] Various, Vectran - Liquid Crystal Polymer Fiber Technology, Technical Report, Kuraray Co. Ltd., Tokyo, Japan, 2014.

[63] D.Y. Limeneh, K.T. Yilma, Misc review on vectran-super fiber from thermotropic crystals of rigid-rod polymer, J. Eng. 2021 (1) (2021) 646148.

[64] C.E.D. Riboldi, F. Gualdoni, An integrated approach to the preliminary weight sizing of small electric aircraft, Aerosp. Sci. Technol. 58 (2016) 134–149. https://doi.org/10.1016/j.ast.2016.07.014

[65] C.E.D. Riboldi, L. Trainelli, A. Rolando, L. Mariani, Predicting the effect of electric and hybrid electric aviation on acoustic pollution, Noise Mapp. 7 (2020) 35–36. https://doi.org/10.1515/noise-2020-0004

[66] University of Illinois Urbana-Champaign, UIUC airfoil coordinates database - m-selig.ae.illinois.edu, accessed Jan. 2026.